Harnessing Methyl Jasmonate Epigenetic Defense Modulation through an Autonomous Robotic Precision Spraying System for Targeted Pest Control

Bennett Huang, Jason Pan

Langley High School, McLean, Virginia, USA

*both authors contributed equally, names are listed alphabetically

Abstract

Agricultural pests are responsible for over 40% of global crop losses. However, traditional pesticides are highly harmful to the environment, detrimental to human health, and are inaccessible for poor farmers. Furthermore, current application methods—either wasteful mass spraying which pollutes the environment or inefficient hand spraying—demand technological innovation. This research proposes a fundamentally new alternative for sustainable crop protection with two main objectives: developing a sustainable, effective alternative to traditional pesticides and engineering an autonomous vehicle interface for precise, targeted deployment.

In the first phase of our project, Methyl Jasmonate (MeJA), a naturally occurring volatile defense hormone was investigated as a sustainable defense elicitor. Although initial trials proved that MeJA effectively deters herbivores, a severe physiological penalty was discovered: upregulating defense concurrently upregulates the *GA2ox* pathway, catabolizing growth hormones, stunting development. To resolve this yield penalty, we developed a transient, spray-induced gene silencing (SIGS) system. We designed chimeric double-stranded RNA (dsRNA) to knockdown growth suppressing enzymes and synthesized positively charged carbon dot (CD) nanocarriers to facilitate cell wall penetration and nuclease protection.

In the second phase, we developed an autonomous vehicle to precisely deploy MeJA, as the dose-sensitivity of the dsRNA/CD-MeJA cocktail demands a high level of precision. For insect identification, we designed a custom detection pipeline using SIFT-based keypoints and a YOLOv5-inspired network to recognize small pests accurately in real-time. This approach overcomes the challenge of detecting small scale pests in high noise agricultural environments. The vehicle utilizes an engineered cam-motor sprayer to deliver precise pulses of the treatment only when pests are identified, operating across the field for durations of up to 12 hours.

Overall, our unified system presents an eco-friendly, effective, and scalable solution that significantly saves resources and time.

1 Introduction

According to the Food and Agricultural Organization (FAO), pests and their associated plant diseases account for up to 40% of global crop losses **(figure 1)**, representing hundreds of billions of dollars in economic damage. As our rapidly growing population places an increasing demand on food supply and economic stability, pest mitigation has turned into a primary challenge for modern agriculture.

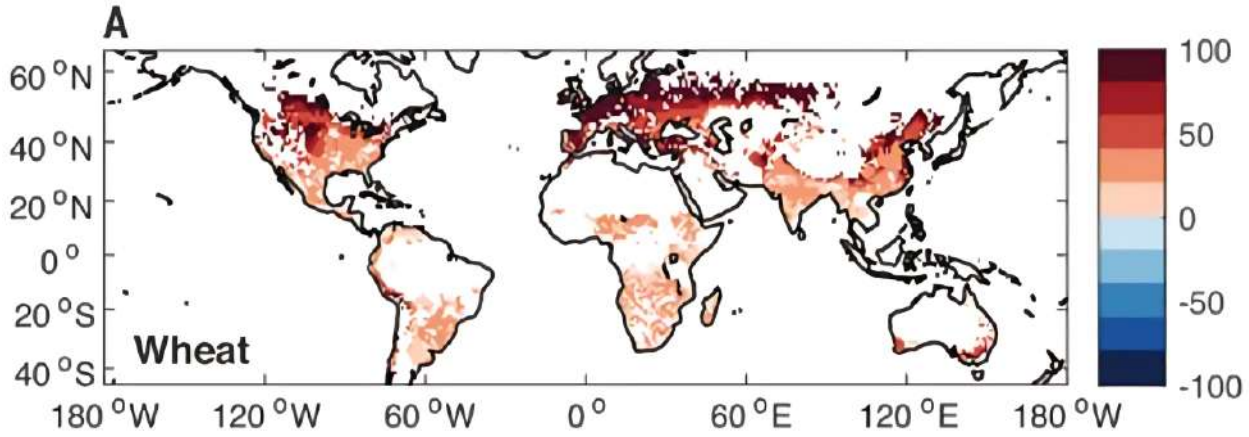


Figure 1: Projected distribution of changes in pest-related crop losses for wheat, where red shows increased losses in future years

Source: Reproduced from Deutsch et al., 2018

Current pest-management strategies rely almost exclusively on the mass-spraying of synthetic chemical pesticides. While effective, these chemicals are catastrophic for environmental health, contributing to soil degradation, water contamination, and chronic human illnesses. To mitigate these risks, the industry has turned toward "precision agriculture." However, current high-tech solutions, such as drone swarms or GPS-guided industrial tractors often cost tens of thousands of dollars and require robust digital infrastructure, rendering them inaccessible to most farmers around the world.

A promising biological alternative to traditional pesticides is Methyl Jasmonate (MeJA), a volatile organic compound naturally produced by plants to trigger internal defense mechanisms. While MeJA is non-toxic and highly effective at deterring herbivores, its agricultural applications have been bottlenecked by a fundamental issue, the growth-defense tradeoff: application often triggers a systemic hormonal response that stunts plant growth, reducing yield. Furthermore, MeJA's high volatility and dose-sensitivity require a level of application precision that manual labor cannot provide.

We propose a novel, interdisciplinary solution to these challenges. We present a dual-phase system that first uncouples the growth-defense tradeoff through the use of carbon dot (CD) delivered dsRNA, and second, deploys this solution via an autonomous robotic vehicle. By combining epigenetic defense modulation with real-time pest detection, this project offers an environmentally sustainable alternative to traditional chemical pest management.

2 Defense Modulation

We first sought out an environmentally sustainable while still effective and affordable alternative to traditional pesticides. We identified Methyl Jasmonate (MeJA), a volatile organic compound and a derivative of the lipid-based hormone jasmonic acid (JA), as a primary candidate for modulation. In nature, MeJA functions as a critical signaling molecule that regulates plant responses to biotic stresses, particularly necrotrophic pathogens and herbivorous insects. When a plant is overwhelmed by insect stress, it biosynthesizes JA, which is methylated into volatile MeJA to signal not only distal parts of the same plant but also neighboring plants to activate their defense systems.

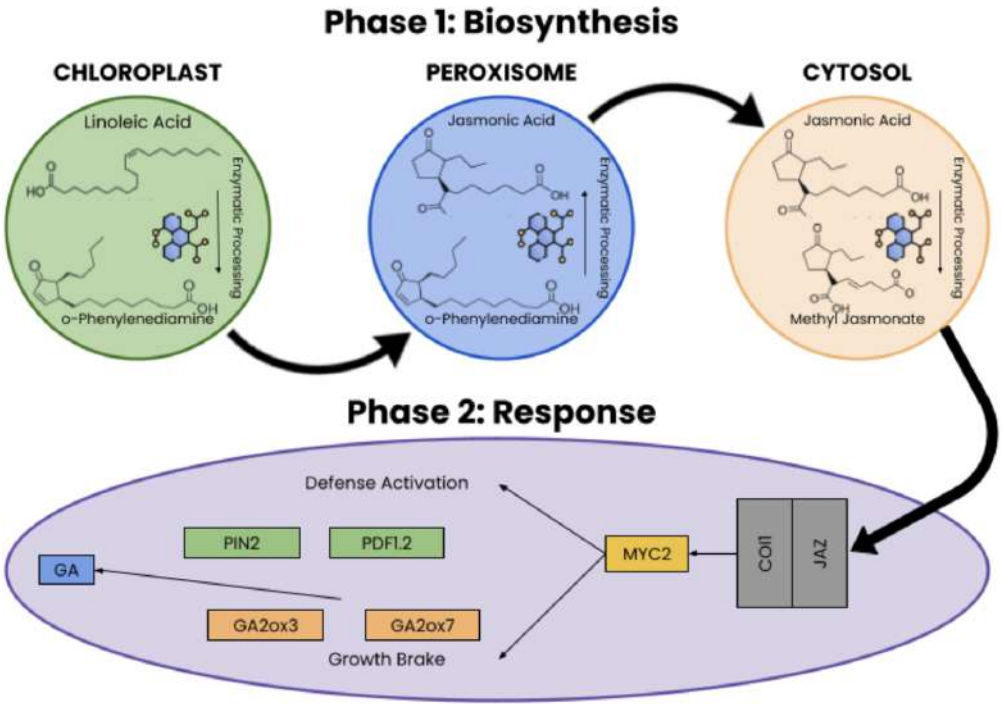


Figure 2: MeJA Synthesis and Pathway

MeJA operates via the COI1-JAZ pathway **(figure 2)**. Under low-stress conditions, the expression of defensive genes is actively repressed by Jasmonate ZIM-domain (JAZ) proteins, which bind to and inhibit transcription factors such as *MYC2*. When cellular levels of Jasmonoyl-L-isoleucine (JA-Ile), the active form of JA, rises due to stress or exogenous application, the hormone binds to the F-box protein COI1 (Coronatine Insensitive 1). This complex then targets the JAZ repressors for ubiquitination and degradation by the 26S proteasome. The destruction of JAZ releases the *MYC2* transcription factors, allowing them to activate the expression of defense-related genes (proteinase inhibitors, glucosinolates, etc). Crucially, this same pathway simultaneously triggers the repression of growth-promoting hormones, specifically gibberellins, by upregulating catabolic enzymes such as GA2-oxidase 3 and 7 (*GA2ox3*, *GA2ox7*), resulting in the reallocation of metabolic resources from growth to defense.

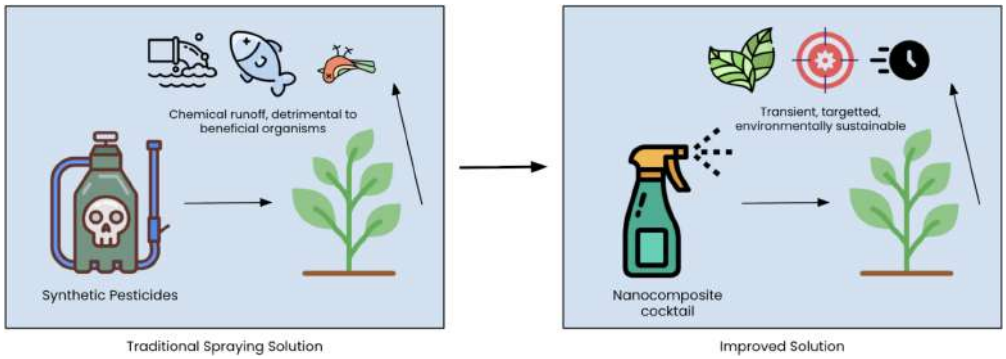


Figure 3: Overview of Spraying Solution

The initial phase of our study **(figure 3)** focused on quantifying the defensive capability of exogenously-applied MeJA against biotic stressors in an agricultural crop model, Cabbage (*Brassica oleracea*). To establish a baseline for efficacy, *Brassica* plants were treated with varying concentrations of MeJA and subsequently challenged with two common agricultural pests: Aphids (*Myzus persicae*) and White Cabbage Caterpillars (*Pieris rapae*). We evaluated the effectiveness of the treatment by measuring four key physiological and ecological variables: (1) Leaf Area Damage, quantified via pixel-based image analysis; (2) Insect Population Count, to measure direct deterrence and mortality; (3) Plant Height Change, to capture the impact on vertical growth patterns in the *MYC2-GA2ox3/7* pathway; and (4) Plant Biomass, to assess the overall "fitness cost" or yield penalty associated with the treatment. This phase confirmed that although MeJA significantly reduced pest pressure and damage, it concurrently imposed a severe penalty on plant growth, validating the existence of a strong growth-defense tradeoff, especially at higher concentrations.

Building on these findings, the second phase of our project aimed to engineer a solution to the observed growth penalty using the model organism *Arabidopsis thaliana* to allow for precise genetic targeting. We hypothesized that the growth-suppression side effect of MeJA is mediated primarily by the upregulation of Gibberellin 2-oxidase 3 and 7 (*GA2ox3*, *GA2ox7*), an enzyme that catabolizes active growth hormones. To rescue plant growth without sacrificing defense, we designed a spray-induced gene silencing (SIGS) system to transiently knockdown *GA2ox3/7* expression during the MeJA response. This phase involved the synthesis of long double-stranded RNA (dsRNA) targeting *Arabidopsis thaliana GA2ox3* and *GA2ox7*, which was then complexed with positively charged Carbon Dot (CD) nanocarriers **(figure 4)** to facilitate cell wall penetration and protection from RNA's inherent instability and environmental nucle-

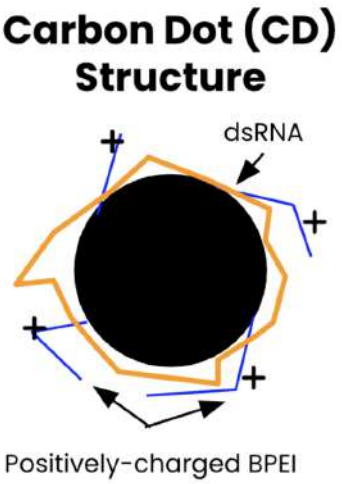


Figure 4: Positively-charged CDs

ases. Efficacy was evaluated by co-applying the CD-dsRNA nanocomplex with MeJA and measuring the rescue of internode elongation and biomass accumulation relative to MeJA-only controls.

2.1 Materials and Methods

2.1.1 Plants and Insects

This study utilized two distinct plant species to evaluate pest deterrence and molecular growth rescue, respectively. To ensure the statistical robustness of the data, all efficacy trials and molecular validation assays were conducted over three independent experimental trials. All subsequent data presented in this study represent the mean values derived from the three trials.



Figure 5: Cabbage Prior to Spraying

For phase 1 (Insect Efficacy), *Brassica oleracea* (Cabbage) seeds were sown in standard potting soil and cultivated in a controlled environment chamber (22–23°C, 55% ± 5% RH, 16-h light/8-h dark photoperiod). Plants were grown for approximately 4 weeks until reaching the true leaf phase prior to insect challenge **(figure 5)**.



Figure 6: Transferring Seeds via Micropipette (left); *Arabidopsis thaliana* Prior to Spraying (right)

For phase 2 (Molecular Rescue), *Arabidopsis thaliana* (Ecotype Col-0) was utilized. To ensure uniform germination, seeds were stratified at 4°C for 72 hours on a moist paper

towel in the dark. Following cold stratification, seeds were sown via liquid suspension using a micropipette onto standard potting soil within individual growth cells **(figure 6, left)**. Experiments were initiated once plants reached the rosette phase (approximately 4 weeks post-germination, 10–12 fully expanded leaves), corresponding to the vegetative to bolting transition phase **(figure 6, right)**.

Plants were cultivated in a controlled environment chamber under long-day conditions (16-h light/8-h dark photoperiod) to promote vegetative growth. Ambient temperature was maintained between 22–23°C with a relative humidity of 55% ± 5%. Plants were watered via moist spraying about twice a day to maintain consistent soil moisture. Experiments were initiated once plants reached the rosette phase (approximately 4 weeks post-germination, with 10-12 fully expanded leaves), corresponding to the vegetative to bolting transition phase.

To evaluate the efficacy of MeJA against insects while controlling for the compound's high volatility, a custom testing tank was engineered. The system consisted of physically isolated compartments designed to prevent volatile organic compound (VOC) crosstalk between treatment groups **(figure 7)**. This isolation was crucial to ensure that control plants were not inadvertently "primed" by MeJA vapors from adjacent treated plants.

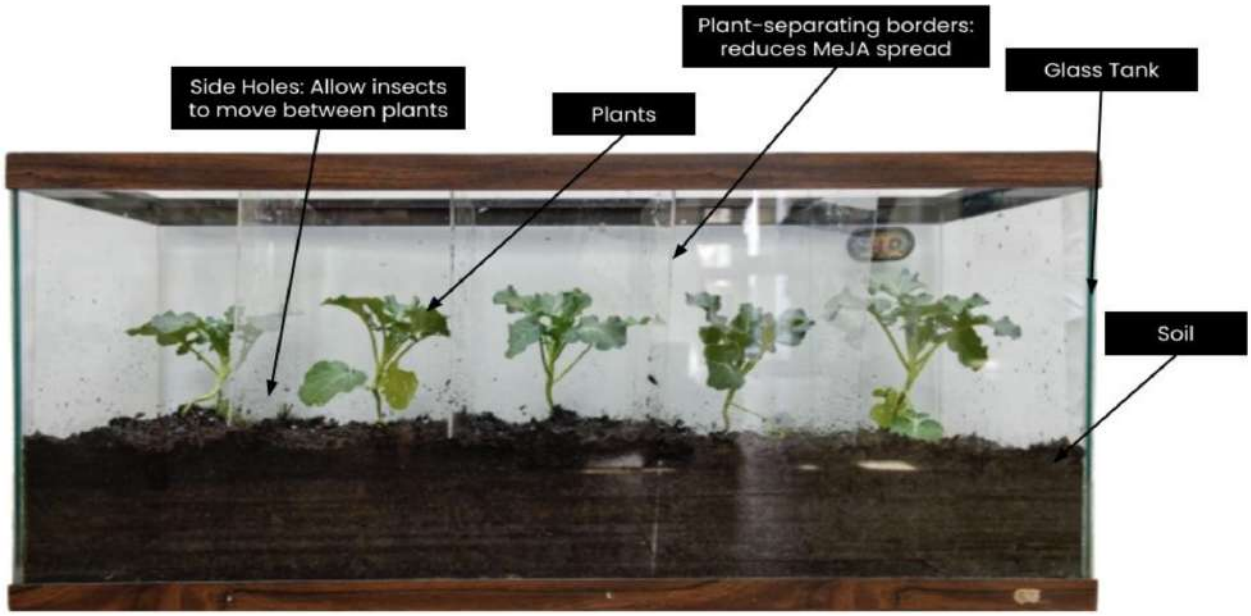


Figure 7: Custom Testing Tank to Prevent MeJA Crosstalk

Two herbivores were utilized for the phase 1 trials: the chewing herbivore Cabbage White Caterpillar (*Pieris rapae*) and the phloem-feeding Aphid (*Myzus persicae*). *Pieris rapae* larvae were sourced commercially, while *Myzus persicae* colonies were obtained from Colorado State University. Insects were introduced to the experimental tank immediately upon the plants reaching the appropriate growth phase. A fixed number of caterpillar larvae or aphids were transferred to each plant **(figure 8)**.



Figure 8: Aphid and Caterpillar Larvae on Plants

2.1.2 Synthesis, Purification, and Characterization of Carbon Dot Nanocarriers

For phase 2, cationic carbon dots (CDs) were synthesized via a bottom-up hydrothermal carbonization method using glucose as the carbon source and branched polyethylenimine (bPEI) as the surface passivation agent. Briefly, 2.0 g of D-glucose and 2.0 g of bPEI (MW 2000) were dissolved in 10 mL of deionized water and mixed until fully homogenized **(figure 9)**. The solution was then transferred into a 50 mL Teflon-lined stainless steel hydrothermal autoclave reactor. The reactor was sealed and heated in a laboratory oven at 180°C for 4 hours to induce carbonization.



Figure 9: Mixing D-glucose with bPEI

The bPEI utilized as a passivation agent is a highly branched polymer characterized by a dense network of primary, secondary, and tertiary amine groups. Under the aqueous conditions of the synthesis, the amine groups underwent protonation, resulting in a cationic surface charge. This positive charge is critical for the nanocarriers' function, as it facilitates a strong electrostatic attraction with the negatively charged phosphate groups on dsRNA. Upon mixing, this attraction creates a "condensation" process, where the elongated, flexible RNA molecules are compressed and coiled tightly around the carbon dot cores to form nanocomplexes. By neutralizing the negative charge of the RNA and providing steric hindrance with its polymer shell, the bPEI coating masks the genetic payload from recognition by RNases, while also reducing the complex's volume to a scale capable of traversing the plant cell wall. Once within the cell, the dsRNA is released through competitive displacement by other anionic cellular components and the proton sponge effect, where the high buffering capacity of the bPEI amine groups facilitates endosomal escape and the unloading

of the genetic payload.



Figure 10: CD centrifugation to remove heavier pellets

Following synthesis, the reactor was allowed to cool naturally to room temperature. The resulting dark yellow/brown solution underwent a two-step purification process to ensure biocompatibility and size uniformity. First, the mixture was centrifuged to remove heavier carbonaceous aggregates **(figure 10)**. Next, the solution was filtered through a 0.2 micron syringe filter. The purified CD solution was stored at 4°C for long-term storage, and fluorescent properties were confirmed via visual inspection of fluorescence under UV light excitation.

2.1.3 In Vitro Synthesis of dsRNA and CD Incorporation

Name	Best Hit (Accession No.)	Percent Identity (%)	Query Coverage (%)	E-Value	Predicted RNAi Efficacy
Thale Cress (Arabidopsis Thaliana)	At GA2ox (NM_103976.2)	100.0%	100%	0.0	High (Reference)
Cabbage	Chromosome 5 (CM068049.1)	83.82%	67%	4e-78	Moderate/High
Broccoli	Chromosome 5 (CM068067.1)	84.19%	67%	9e-80	Moderate/High

Figure 11: *GA2ox* Conservation Across a Family

For phase 2, target sequences for *Arabidopsis thaliana GA2ox7* and *GA2ox3* were identified using the NCBI RefSeq database. To minimize off-target effects while maximizing silencing efficacy, a chimeric sequence containing 200 bp regions from the coding sequences

of both genes was designed. Specificity was verified using NCBI BLASTn to ensure no significant homology to non-target genes, particularly the growth-promoting *GA2ox* family. Furthermore, BLASTn analysis against the *Brassica oleracea* genome revealed high sequence conservation (83% identity) in the targeted regions, especially among the *Brassica* family, which includes kale, cabbage, and turnips, suggesting potential translational applicability of this RNAi construct to various cruciferous crops **(figure 11)**. The final dsRNA template, flanked by T7 promoter sequences on both 5' and 3' ends, was synthesized as a double-stranded DNA gBlock **(figure 12)**.



Figure 12: *GA2ox3* and *GA2ox7* Chimeric Sequences

Prior to transcription, the gBlock templates were amplified via Polymerase Chain Reaction (PCR) to generate sufficient transcriptional substrates. Amplification was performed using DNA polymerase and a universal primer targeting the flanking T7 promoter sequence (TAATACGACTCACTATAGGG). The resulting PCR amplicons were purified using ethanol precipitation for DNA purification to remove excess primers and salts, quantified via NanoDrop and gel electrophoresis and utilized as the linear template for RNA synthesis.

Double-stranded RNA was synthesized using a High-Yield T7 RNA Transcription Kit. The DNA template was resuspended in nuclease-free water to a concentration of 50 ng/µL. Transcription reactions were assembled according to the manufacturer's protocol **(figure 13)** and incubated at 37°C for 4 hours. Following transcription, the reaction was heated to 85°C for five minutes and allowed to cool slowly to room temperature over 30 minutes to facilitate the annealing of complementary RNA strands into stable dsRNA.



Figure 13: RNA Synthesis Using T7 Kit

The DNA template was subsequently removed by digestion with DNase I at 37°C for 15 minutes. The resulting dsRNA was purified using a silica-column RNA purification kit **(figure 14)** and quantified via NanoDrop spectrophotometry. Integrity and length were subsequently verified by agarose gel electrophoresis.

CD-dsRNA nanocomplexes were formed via electrostatic self-assembly. Purified Carbon Dots and dsRNA were mixed in nuclease-free water at a 2:1 mass ratio (CD:dsRNA) and vortexed immediately. The mixture was incubated at room temperature for 20 minutes to allow the positively charged bPEI surface of the CDs to bind and condense the negatively charged dsRNA. A non-ionic surfactant (Tween-20, 0.1% v/v) was added to the final formulation to facilitate spreading and stomatal entry.

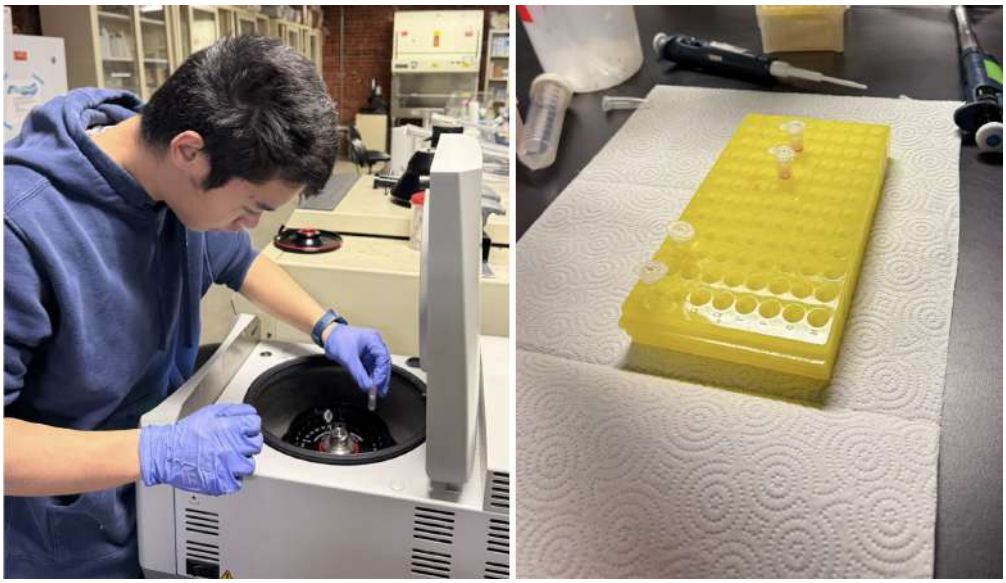


Figure 14: Spin-column purification of RNA

The stability and binding efficiency of the nanocomplexes were validated through two assays. First, an Electrophoretic Mobility Shift Assay (EMSA) was performed on a 1% agarose gel; retention of the RNA fluorescence in the well indicated successful binding and charge neutralization by the CDs. Secondly, an RNase protection assay was conducted by incubating naked dsRNA and CD-dsRNA to assess degradation.

2.1.4 Spray Application and Quantitative Data Characterization

For phase 2, *Arabidopsis thaliana* plants were treated at the onset of bolting (approximately 4 weeks post-germination) to evaluate the efficacy of the CD-dsRNA/MeJA co-application. A 2X Master Mix strategy was utilized to ensure consistent concentrations across all treatment groups **(figure 15)**. A 2X RNA Master Mix was prepared by combining 1 mL of dsRNA stock (2000 ng/µL), 2 mL of Carbon Dot stock (2000 ng/µL), and 17 mL of nuclease-free water, yielding a solution with 100 ng/µL of dsRNA and 200 ng/µL of CDs. Similarly, 2X Methyl Jasmonate stock solutions were prepared via serial dilution from a 1M MeJA-ethanol stock to produce 200 µM and 2000 µM working solutions.

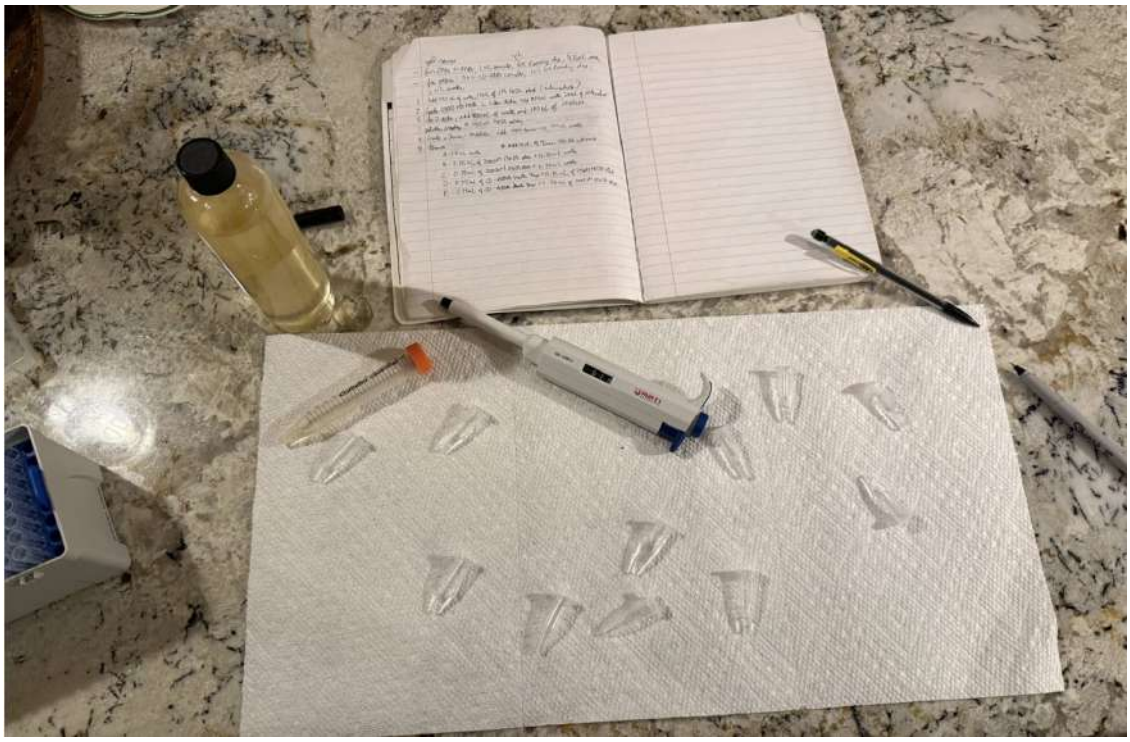


Figure 15: Treatment Preparations for RNA

Plants were divided into five treatment groups (A-E) with distinct spray formulations, with 10 mL total volume per group **(figure 16)**. All formulations were supplemented with 0.1% (v/v) Tween-20 immediately prior to application to facilitate stomatal flooding:



Figure 16: Sample from Cohort Groups A-E

Cohort Groups:

- (A): mock control, water + surfactant
- (B): low cocktail, 100 µM MeJA + 50 ng/µL CD-dsRNA (5 mL 200 µM MeJA + 5 mL 2X RNA Mix)
- (C): high cocktail, 1000 µM MeJA + 50 ng/µL CD-dsRNA (5 mL 2000 µM MeJA + 5 mL 2X RNA Mix)
- (D): low MeJA, 100 µM MeJA (5 mL 200 µM MeJA + 5 mL water)
- (E): high MeJA, 1000 µM MeJA (5 mL 2000 µM MeJA + 5 mL water)



Figure 17: Treatment Application Using Brush

Treatments were applied using a brush to the leaf surfaces until runoff **(figure 17)**. Physiological responses were monitored over a 7-day period post-treatment. Morphological metrics included internode length, total plant height, and % change in fresh shoot biomass.

2.1.5 Leaf Area Measurement

For phase 1, leaf area loss was quantified to evaluate the efficacy of MeJA as a feeding deterrent. Herbivore damage was assessed by measuring the reduction in total foliar surface area. A non-destructive, pre-post imaging method was not feasible for attached leaves; thus, a representative sampling strategy combined with digital image segmentation was utilized to estimate biomass loss.

Prior to insect infestation, a reference cohort of undamaged, age-matched *Brassica* leaves were harvested to establish a baseline mean leaf area. Leaves were photographed individually on a high-contrast background using a fixed focal length and camera height to ensure consistent pixel density **(figure 18, left)**. A reference scale marker of known dimensions was included in each frame, facilitating the conversion of pixel counts to physical area (cm^2).

Image processing was performed using a custom color-thresholding algorithm. The algorithm segmented the leaf tissue from the background based on hue and saturation parameters specific to the leaf color **(figure 18, right)**. The total pixel count of the segmented region was converted to surface area, and the mean value of this reference was established as the estimated initial area ($A_{initial}$) per leaf.

Following the insect exposure period, all leaves from the original plants that were subject to herbivory were harvested and imaged using the identical setup described above. The remaining surface area of each leaf (A_{final}) was computed via the same segmentation pipeline. Total herbivory damage (A_{loss}) for each plant was calculated as the difference between the estimated initial area and the measured final area. This metric provided a quantitative measurement for insect feeding activity, independent of subjective visual scoring.



Figure 18: Camera setup for consistent image scales (left), original image of a leaf (middle), and computer processed leaf image with its calculated area in pixels (right)

2.2 Results

2.2.1 Validation of MeJA Pest-Deterrence Efficacy and Growth Tradeoffs in *Brassica oleracea*

To validate the defensive utility of Methyl Jasmonate (MeJA) in an agricultural setting, *Brassica oleracea* plants were challenged with *Pieris rapae* (White Cabbage Caterpillar;

chewing herbivore) and *Myzus persicae* (Aphid; phloem-feeding herbivore).

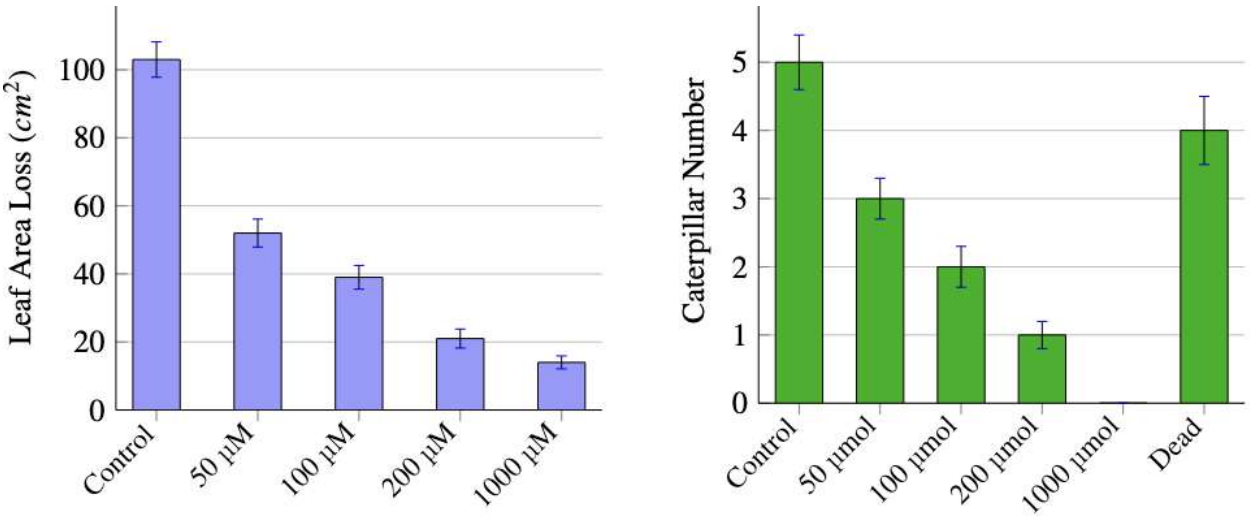


Figure 19: Leaf Area Loss & Caterpillar Count vs. MeJA Solutions

Treatment with MeJA significantly reversed this trend. Even at a moderate concentration of 100 µM, leaf area loss was reduced by over 62% (to 39 cm^2), and the surviving caterpillar population dropped to 2 larvae. At the highest concentration tested (1000 µM), the protection was nearly absolute: leaf area loss was minimized to just 14 cm^2 (an 86% reduction compared to control), and zero caterpillars survived. Finally, a substantial percentage of the insects (25%) were killed by the MeJA spray. This confirms that MeJA is a highly effective biopesticide against chewing insects **(figure 19)**.

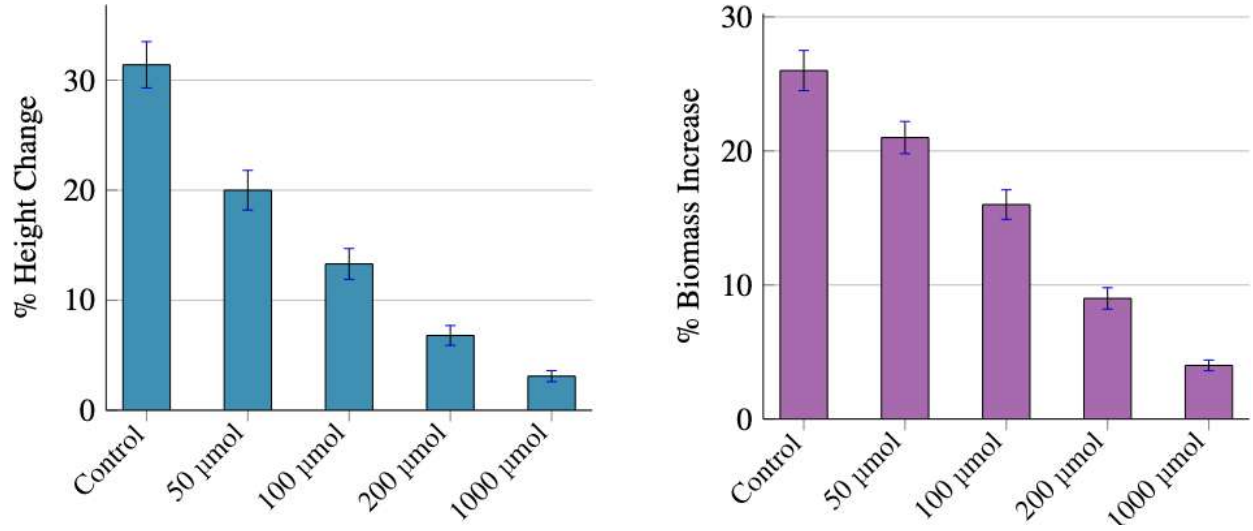


Figure 20: % Height Change vs. % Biomass Increase

However, the physiological cost of this chemical defense was substantial. As MeJA concentration increased, vertical plant growth was progressively inhibited. While control plants grew vigorously, increasing their height by 31.4% over the trial period, plants treated with

the highly effective 1000 µM dose exhibited severe stunting, with a height increase of only 3.1%. This represents a ten-fold reduction in growth rate compared to the untreated plants. Intermediate doses showed a linear dose-response relationship (e.g., 100 µM yielded 13.3% growth), confirming that the mechanism protecting the plant from herbivory is directly linked to the suppression of vegetative growth **(figure 20)**.

2.2.2 CD-dsRNA Nanocomplex Validation

Following Phase 1 confirmation that MeJA effectively deters pests but incurs a significant biomass penalty, Phase 2 focused on validating the molecular components of the growth-rescue system. This was conducted in three distinct stages: amplifying and verifying the DNA gBlock template, quantifying the synthesized dsRNA payload, and characterizing the functional capacity of the CD nanocarriers.

Prior to transcription, the DNA sequence was rigorously established. Target sequences for *GA2ox7* and *GA2ox3* were identified and synthesized into a chimeric sequence designed to maximize silencing efficacy while minimizing off-target effects. This chimeric DNA template, flanked by T7 promoter sequences, was synthesized as a DNA gBlock.

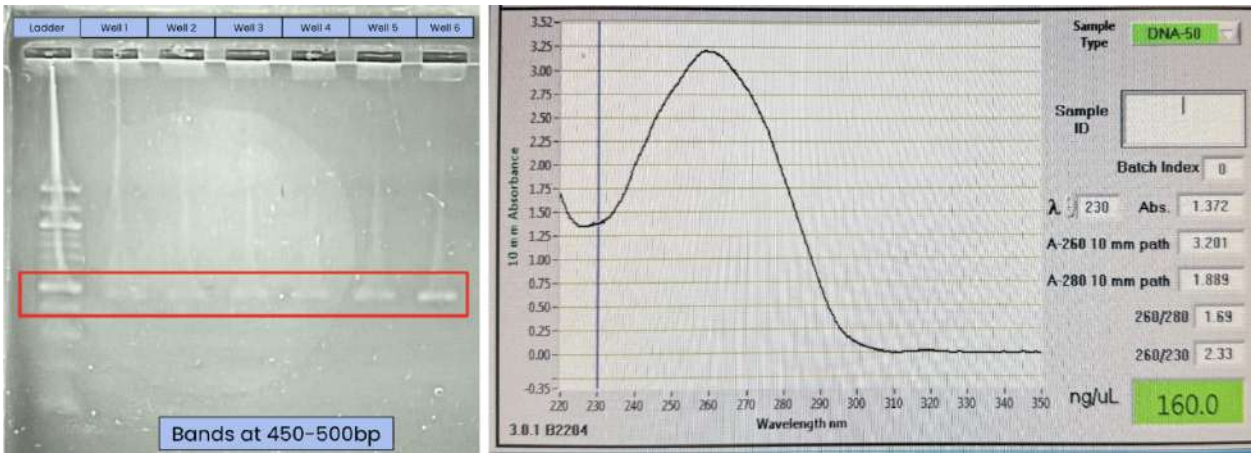


Figure 21: Gel confirmation of DNA amplification (left); Nanodrop measurement of DNA Concentration (right)

To generate sufficient transcription templates, the gBlock was amplified via PCR using universal primers targeting the T7 promoter (TAATACGACTCACTATAGGG). The success of this amplification was confirmed through gel electrophoresis, which revealed clear, distinct bands between 450-500 bp **(figure 21)**, precisely matching the expected size of the sequence. Quantitative analysis via NanoDrop spectrophotometry confirmed a high DNA recovery of 160.0 ng/µL **(figure 22)**.

Using the validated DNA template, dsRNA was synthesized via a High-Yield T7 RNA Transcription Kit. Following a four-hour incubation at 37°C and subsequent DNase I digestion to remove the DNA template, the resulting dsRNA was purified using a silica-column purification kit.

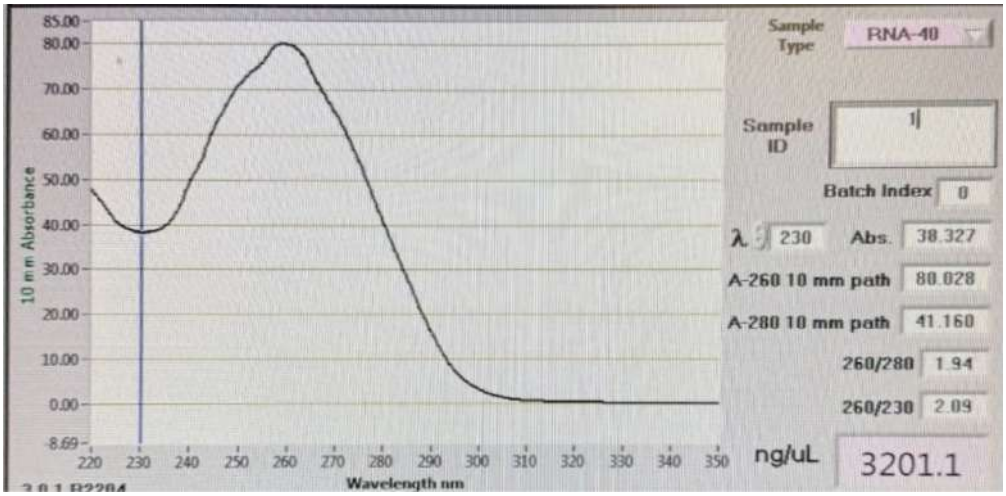


Figure 22: dsRNA Characterization Using NanoDrop

The validation of the RNA payload was performed using NanoDrop spectrophotometry and gel electrophoresis. NanoDrop results showed an exceptionally high yield of 3201.1 ng/µL, critical for ensuring adequate concentration for field-scale spraying. The 260/280 purity ratio of 1.94 indicated minimal protein contamination and high chemical integrity **(figure 22)**.

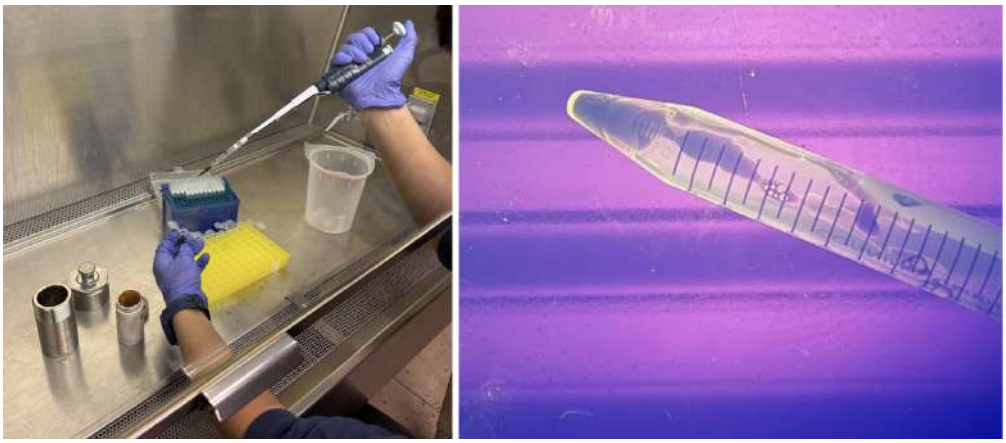


Figure 23: Crude Purification of CDs (left); Validation of CD Synthesis Using UV Excitation (right)

To facilitate dsRNA delivery, CDs were synthesized through a bottom-up hydrothermal carbonization approach. Utilizing glucose as the carbon source and bPEI as the passivation agent, the mixture was heated at 180°C for four hours. The bPEI chains were incorporated onto the carbon core, conferring a strong positive surface charge and high hydrophilicity. The crude solution underwent a purification process, centrifuged to remove large aggregates, keeping the supernatant **(figure 23)** and then filtered through a 0.2-micron membrane. Synthesis validity was verified through UV-light excitation, where the CDs displayed clear fluorescence **(figure 23)**.

The functional capacity of the CDs to bind and protect dsRNA was assessed via gel electrophoresis.

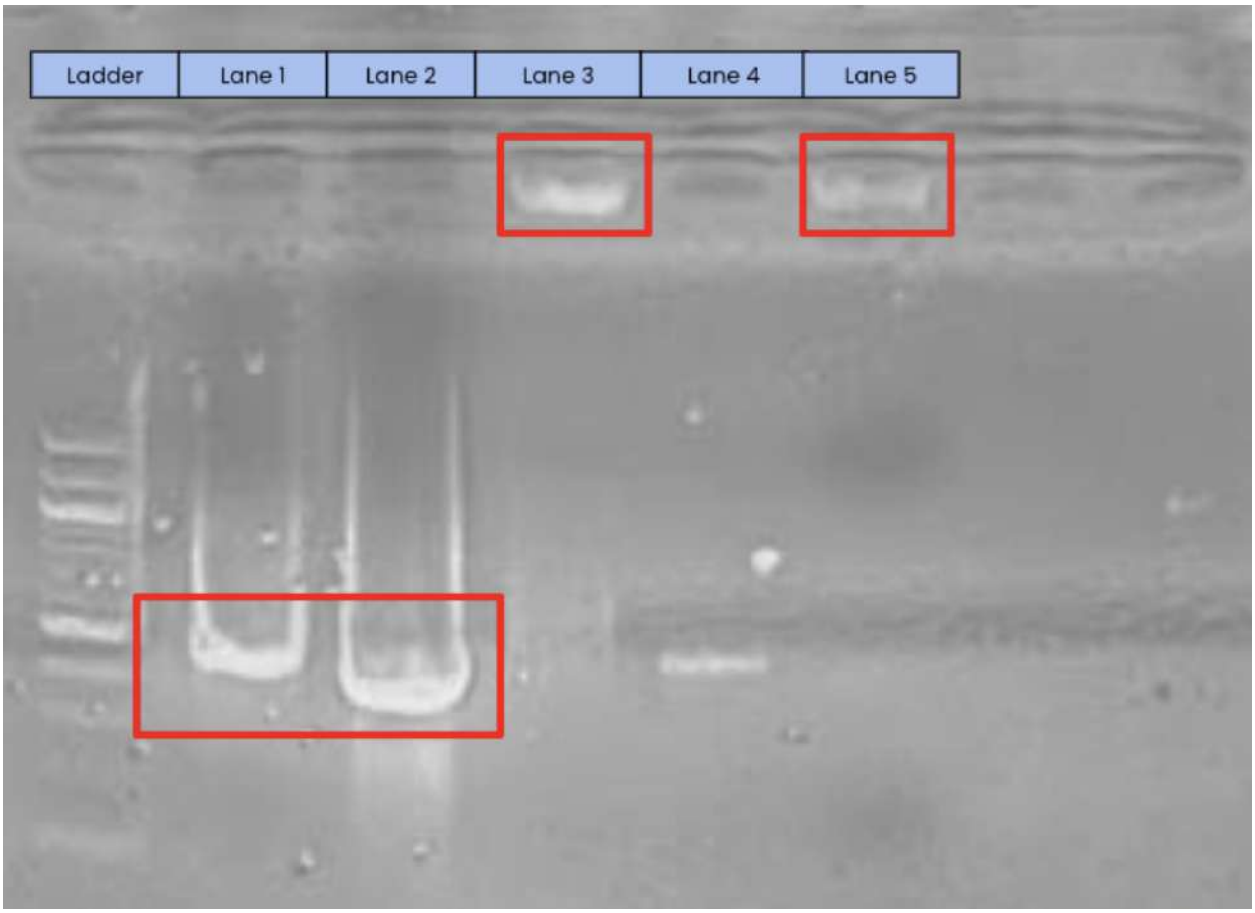


Figure 24: dsRNA Gels

Firstly, dsRNA length was validated, and a clear band appeared at the 450-500bp marker, corresponding to the correct length **(figure 24, lanes 1-2)**. Secondly, an Electrophoretic Mobility Shift Assay was performed to determine the optimal binding ratio. At a mass of 2:1 (CD:dsRNA), the electrophoretic migration of the dsRNA was completely retarded, with fluorescence retained in the loading well **(figure 24, lane 3)**. This indicates that the cationic CDs successfully neutralized the anionic charge of the dsRNA, which subsequently indicates stable, condensed nanocomplexes. Critically, the protective capability of the bPEI shell was evaluated using an RNase protection assay. Upon exposure to RNase A (10 mg/mL) for 30 minutes at 37°C, naked dsRNA controls were mostly degraded, resulting in the absence of a band in the gel **(figure 24, lane 4)**. In contrast, dsRNA complexed with CDs remained intact, appearing as a distinct band comparable to the untreated control **(figure 24, lane 5)**. These results demonstrate that the CD nanocarrier effectively shields the genetic payload from enzymatic hydrolysis, a prerequisite for maintaining RNAi efficacy in the RNase-rich environment of the plant leaf surface and apoplast.

2.2.3 Phenotypic Rescue of Plant Growth

Following the synthesis of the CD system, we evaluated the physiological impact of the cocktail (MeJA + CD-dsRNA) spray on *Arabidopsis thaliana*. Treatments were applied at the critical vegetative to bolting transition (4 weeks post-germination) to assess the ability of the treatment to counteract MeJA-induced growth suppression. Cohort groups, as displayed in the below figures are described in-detail in section 2.1.4.

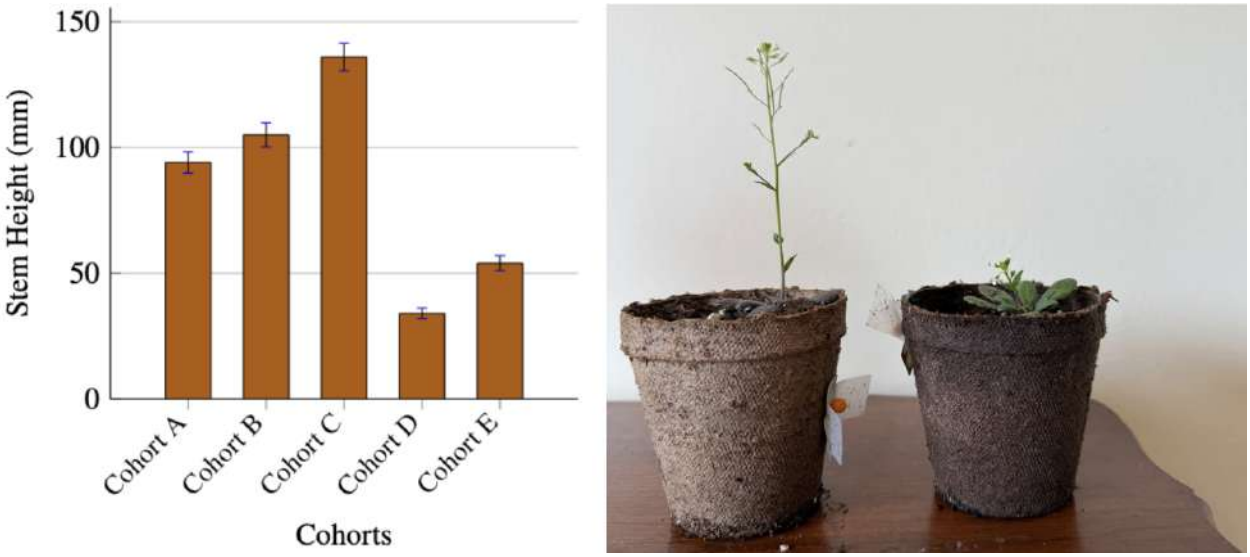


Figure 25: Height Rescue via dsRNA

Consistent with the findings from phase 1, plants treated with MeJA alone exhibited a severe stunted phenotype. This response was characterized by a direct inhibition of bolting, resulting in a compact, rosette-like morphology with shortened internodes. Quantitative analysis revealed that 14 days post-treatment, the MeJA-only group showed a 60.3% reduction in total height at the 100 µM concentration (Cohort D) and a 75% reduction in total height at the 1000 µM concentration (Cohort E) compared to the water-treated controls (Cohort C), confirming the activation of the growth-defense tradeoff **(figure 25)**.

In contrast, co-application of the CD-dsRNA nanocomplex targeting *GA2ox3/7* successfully rescued the growth phenotype. Plants in the cocktail group exhibited rapid internode elongation and vertical growth rates that were statistically superior to the MeJA-only group. Final height measurements indicated that the Cocktail group (Cohort A-B) was approximately 51–60 mm (94–176%) taller than the MeJA-only group, effectively restoring vertical height to levels comparable to the unstressed control group **(figure 26)**.

To assess the impact on overall plant health and potential agricultural yield, fresh shoot biomass was quantified at the conclusion of the trial (Day 7). The chemical defense induction in the MeJA-only group incurred a significant fitness cost, resulting in a 50–60.5% loss in biomass relative to controls.

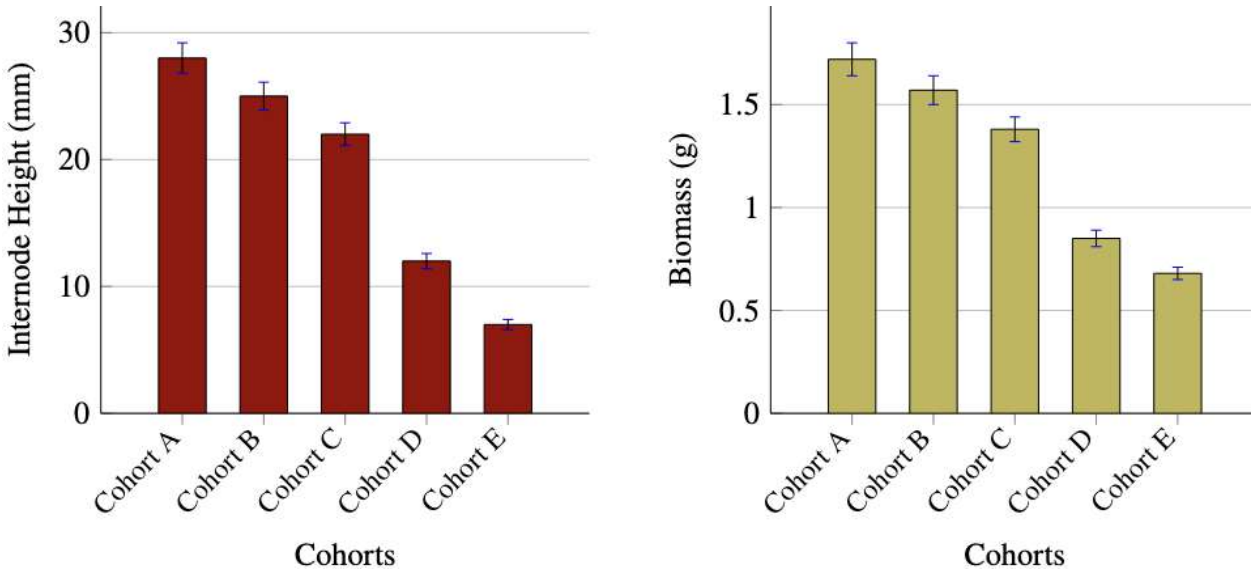


Figure 26: Internode Height and Biomass of Cohort Groups

Crucially, the dsRNA treatment mitigated this penalty. The cocktail group accumulated 84–102.9% more fresh biomass than the MeJA-only group **(figure 26)**. This significant recovery in biomass indicates that the transient silencing of *GA2ox3/7* allowed the plant to maintain carbon allocation towards vegetative structures even in the clear presence of a defense-inducing signal.

2.3 Analysis

2.3.1 Uncoupling the Growth-Defense Tradeoff via Targeted Hormonal Regulation

The central finding of this study is the successful uncoupling of the inverse relationship between plant immunity and vegetative growth, a phenomenon known as the growth-defense tradeoff. In agricultural contexts, the activation of the Jasmonate pathway via chemical elicitors such as Methyl Jasmonate is a potent tool for pest control, but its adoption has been severely limited by the associated yield penalty. Our results demonstrate that this penalty is not an unavoidable metabolic cost, but rather a specific, genetically regulated decision made by the plant.

The mechanism of this tradeoff relies on hormonal crosstalk; the antagonistic interaction between the defense hormone Jasmonate (JA) and the growth hormone gibberellin (GA). Under normal MeJA stimulation, the degradation of JAZ repressors releases *MYC2* transcription factors, which not only activate defense genes such as *Pin2* but directly upregulate *GA2ox3/7*. These enzymes catabolize bioactive gibberellins into inactive forms, essentially hitting the brakes on cell elongation to conserve resources. By selectively silencing *GA2ox3* and *GA2ox7* transcripts via RNA interference, we effectively severed this specific regulatory link.

Our data shows that plants treated with the CD-dsRNA/MeJA cocktail maintained high levels of defense while simultaneously preserving plant height and biomass. By intervening at this specific pathway, we have engineered a plant phenotype that is chemically defended yet physiologically uninhibited, effectively bypassing the evolutionary "decision" to prioritize defense over growth.

2.3.2 Mechanism of Nanocarrier-Mediated Delivery and Stability

The successful phenotypic rescue observed in this study was reliant on the efficacy of the Carbon Dot (CD) nanocarrier system. The delivery of exogenous RNA into plant cells faces two primary barriers that have historically limited the utility of spray-on RNAi: the physical barrier of the cell wall and the biological barrier of environmental nucleases. Our results indicate that the bPEI-passivated CDs effectively overcame both problems.

First, the size exclusion limit of the plant cell wall is estimated to be between 5 and 20 nm, making it impermeable to larger nanoparticles often used in mammals (e.g., liposomes, 50-200 nm). Conversely, our synthesis method produced ultra-small carbon dots. This small size profile suggests that the CDs are capable of passively diffusing through the cell wall to reach the plasma membrane.

Secondly, the phyllosphere and apoplast are rich in RNases designated to degrade foreign viral RNA. Our in vitro protection assays confirm that the Carbon Dots shielded the dsRNA payload. This protection is attributed to the branched polyethylenimine (bPEI) coating. The high density of amine groups on the CD surface not only neutralizes the negative charge of the RNA backbone to form a condensed, nuclease-resistant nanocomplex but also facilitates endosomal escape once inside the cell. This dual function validates bPEI-functionalized Carbon Dots as a superior, low-cost alternative to peptide or lipid-based carriers for agricultural applications.

2.3.3 Advantages of Transient SIGS over Stable Genetic Modification

A critical distinction of our study is the utilization of spray-induced gene silencing (SIGS) rather than permanent genomic editing. While knocking out *GA2ox* could theoretically produce permanently taller plants, such constitutive loss of function mutations often result in deleterious pleiotropic effects. Gibberellins are not only vegetative growth regulators but also essential for floral induction, pollen development, and fruit set. A permanent disruption of GA catabolism could lead to bolting at inappropriate times or reduced reproductive fitness, ultimately harming crop yield.

By utilizing a dsRNA spray, we achieve a transient and tunable gene knockdown. The silencing effect is temporary, persisting only as long as the dsRNA pool remains active within the cell. This allows for a "precision agriculture" approach; farmers can apply the cocktail spray specifically during the early vegetative growth phase—when the plant is most vulnerable to herbivore damage and when rapid biomass accumulation is the most critical. As the plant transitions to reproduction, the silencing effect dissipates, allowing normal

hormonal homeostasis to return for proper flowering and fruiting. This flexibility offers a significant advantage over the "always on" nature of traditional transgenic modifications and avoids the regulatory hurdles associated with GMOs.

2.3.4 Limitations and Future Directions

Although this study successfully established the molecular and phenotypic efficacy of the CD-dsRNA/MeJA system under controlled laboratory conditions, several factors must be addressed for successful translation to field agriculture. Firstly, environmental durability remains a challenge. Our trials were conducted in a growth chamber with stable temperature and no precipitation. In a field setting, UV radiation, rain wash-off, and microbial degradation in the phyllosphere could reduce the active window of the dsRNA spray. Future formulations will likely require the incorporation of stickier substances.

Secondly, this study utilized *Arabidopsis thaliana* as a genetic model because of its widely accessible genome and its short lifespan as a model organism. Although GA and JA signaling pathways are highly conserved across angiosperms, physical barriers to entry differ significantly among crops. Species with thicker waxy cuticles (such as maize, for example) or lower stomatal densities may require modification or the addition of specific surfactants to ensure sufficient uptake.

Finally, a primary limitation of this research phase was the constraint of high laboratory and analysis costs, which precluded the completion of quantitative reverse transcription PCR (RT-qPCR) analysis. Although the phenotypic evidence, specifically the significant rescue of stem elongation strongly supports our hypothesis of *GA2ox* silencing, molecular validation is essential to definitively correlate these physical changes with gene knockdown. Completing this characterization will bridge the gap between our observed phenotypic results and the underlying genetic mechanism.

3 Deployment Vehicle

In this section, we develop an autonomous vehicle for deploying Methyl Jasmonate precisely across entire crop regions **(figure 27)**. As demonstrated in the preceding results, the efficacy of MeJA is highly dose-sensitive; while MeJA provides the necessary defense, over-application is expensive and results in significant vegetative stunting. Consequently, unlike conventional mass-spraying systems, the vehicle was intentionally engineered to spray the MeJA solution only on plants when pests were detected in real-time. Overall, the vehicle is run entirely on edge devices without the need for external connection to make it more accessible and easier to deploy. By processing detection and navigation logic locally, the system operates without the need for high-speed internet or external server connections, making it a viable tool for farmers in remote or resource constrained environments. With a battery life of 10-12 hours, this autonomous system enables continuous, high-precision pest management.

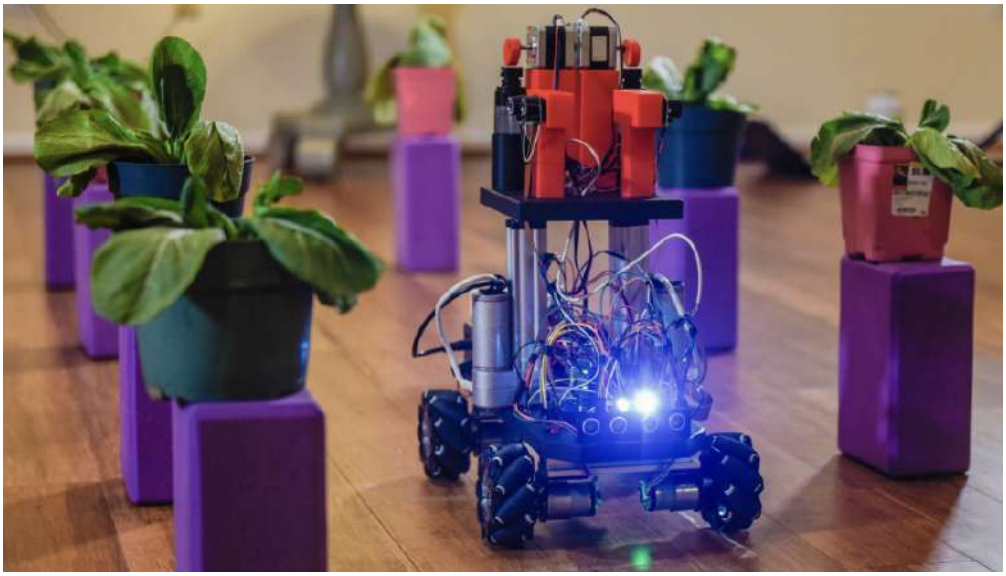


Figure 27: Dual-platform pest-control vehicle carrying out pest management.

The following sections detail the platform's technical architecture and operational logic. Subsection 3.1 describes critical hardware specifications and mechanical design, while Subsection 3.2 describes the autonomous workflow.

3.1 Vehicle Hardware Design

The deployment vehicle is designed as a two-platform system. The lower platform (Platform 1) houses all the essential electronics and executes vehicle movement **(figure 28)**.

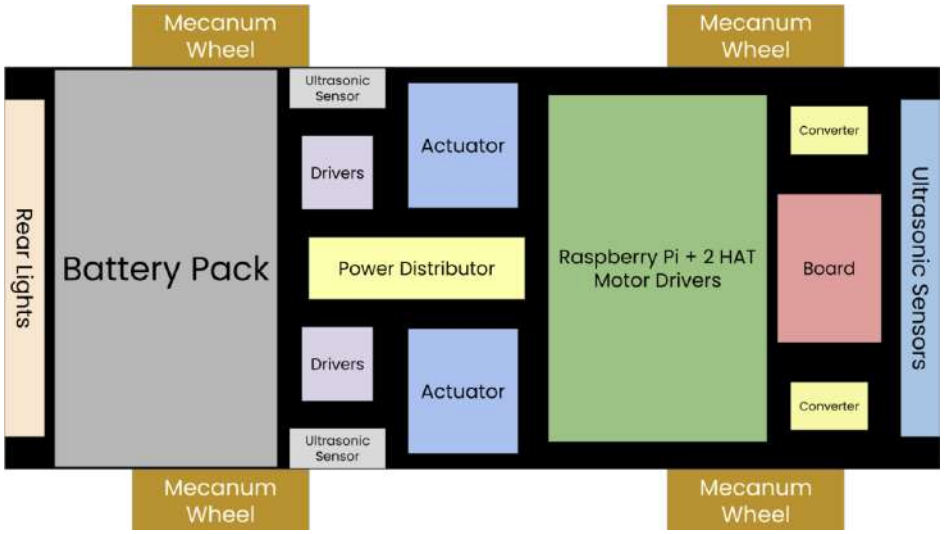


Figure 28: Top view of Platform 1, showing the layout of all the components.

The top platform (Platform 2) was mounted above the lower one and houses the spraying system designed to precisely spray the Methyl Jasmonate solution and precision cameras

for pest-detection. The two platforms are connected by two 12-volt 5-amp VEVOR linear actuators, which allow the upper platform to move vertically. The linear actuators can reach heights of over a full foot from the base, allowing the spraying system (on the second platform) to reach different levels of plant height for smaller crops, resulting in a comprehensive check of the entire field

The vehicle's base utilizes a four-wheel mecanum wheel system for precise movement **(figure 29)**. Mecanum wheels are specialized omnidirectional wheels with angled rollers around the wheel circumference. Because of these angled rollers, each wheel generates force components in both the forward and sideways directions. By coordinating the rotation of all four wheels, the vehicle can rotate in place and laterally shift without changing its orientation. Each wheel is powered by a 12-volt Encoder DC Motor that can generate significant torque. Overall, the use of mecanum wheels allow the vehicle to accurately reposition itself, which is especially important in tight crop environments.

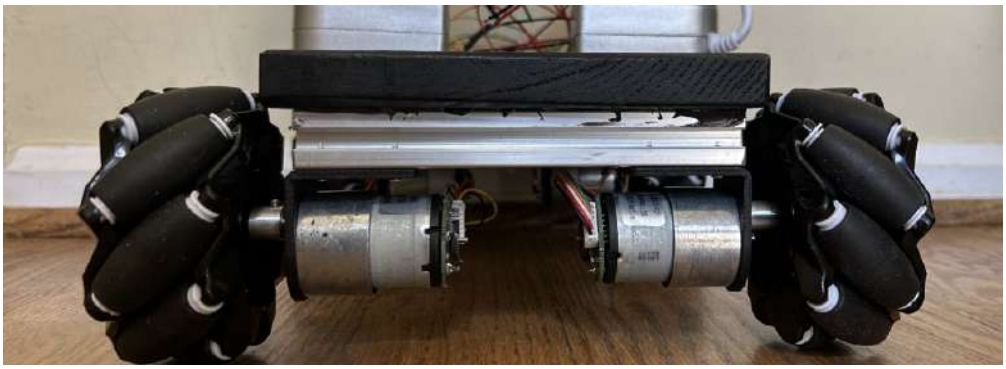


Figure 29: Two mecanum wheels and their motors, highlighting their angled rollers that allow for precise movement

Mounted on the first level of the vehicle are four 3.3-volt HC-SR04 ultrasonic sensors. Ultrasonic sensors use sound waves to detect nearby obstacles and determine how far they are from the vehicle itself **(figure 30)**. Two of the sensors are mounted on the front of the vehicle, and the other two sensors on its left and right. This allows our vehicle to map out open areas and avoid blocked regions by scanning its surroundings for objects. Combining ultrasonic sensors with our mecanum wheels allows the vehicle to move safely throughout the entire field while avoiding obstacles.

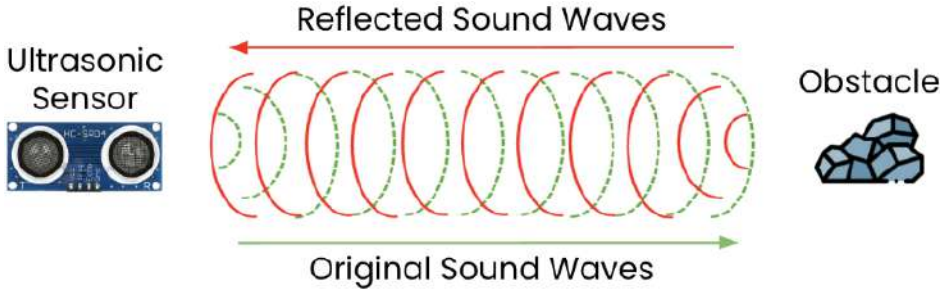


Figure 30: Overview of how ultrasonic sensors work (sending out sound waves)

Because these ultrasonic sensors had a different voltage than what our power systems produced, we used an 8-channel bidirectional logic converter from 5 volts to 3.3 volts to allow them to function properly. The ultrasonic sensors we used require 5-volt logic signals, while the Raspberry Pi's GPIO pins operated at 3.3 volts and could be permanently damaged by higher voltages. The ultrasonic sensors' trigger signals were sent from the Raspberry Pi through the converter to the sensors at 5 volts, while the echo signals gathered by the sensors were stepped down to 3.3 volts before being read by the Raspberry Pi. Because this setup required multiple signal, power, and ground connections that exceeded the available space on the logic converters, we used an EPLZON Printed Circuit Board to organize and manage the wiring.

On the second platform, the vehicle uses two Raspberry Pi V3 camera modules to scan the field and look for pests **(figure 31)**. This specific camera version gives us a large resolution 2304 by 1296 pixels, but more importantly, it has powered autofocus. This allows the camera to better focus and therefore capture objects even with the external vehicle movement going on simultaneously. On the two sides of each Raspberry Pi camera are infrared LED lights that each have an internal light sensor **(figure 32)**. When the environment gets dark, the infrared LED lights will light up, allowing the Raspberry Pi camera to continue detecting pests. This makes the vehicle usable during the day and night.

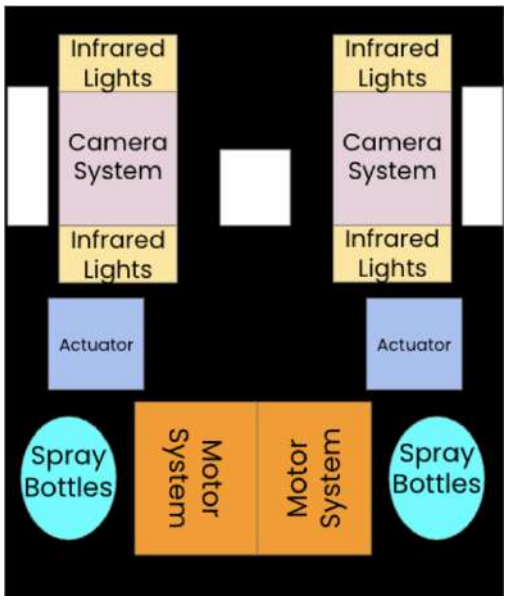


Figure 31: Top view of Platform 2, showing the layout of all the components

Then, once pests are detected, we use a motor-cam spraying system to spray the MeJA solution. The cams are bidirectional and mounted to a 12-volt DC high-torque stepper motor.



Figure 32: Two infrared LEDs (left and right) and a Raspberry Pi camera (middle)

Attached to the motor's shaft is an irregular red cam piece that was custom designed and 3D printed. Below it is the spray bottle containing the MeJA solution **(figure 33)**. Essentially, due to the irregular shape of the cam piece, the cam presses down on the sprayer exactly once each time the motor makes a full rotation, spraying the solution in a controlled manner. By converting the motor's rotational motion to a vertical force that can spray the MeJA, it allows us to accurately control the amount of MeJA sprayed based on the number of times we tell the motor to rotate.



Figure 33: Top platform of the vehicle. Focuses on the two motor-cam spraying systems.

In general, for full autonomous control, we used a Raspberry Pi 5 module to act as the "brain" of the vehicle **(figure 34)**. Every single part of our vehicle eventually wired back to the Raspberry Pi, making it serve as the unifying platform that allowed us to control all parts precisely. To code on the Raspberry Pi, we connected it to an external monitor via an HDMI cable and attached a keyboard as well. On top of the Raspberry Pi, we stacked two Adafruit DC & Stepper Motor HAT drivers. The first HAT driver was responsible for helping control the stepper motors part of the spraying system and the four mecanum wheel motors. The second HAT driver was responsible for helping control the linear actuators and ultrasonic sensors. For the two linear actuators, we used two Adafruit DRV8871 DC Motor Driver Breakout Boards as another intermediary layer to allow for power management and better control.

To power all the components of the vehicle, we used a TenLike power bank of 99.9 watt-hours. This battery is strong enough so that when fully charged, the vehicle is able to operate for 10-12 hours continuously without any human intervention. To accordingly distribute the power to all parts of the vehicle based on their individual power requirements, we used a PCB Double-Layer Wiring 2x12 Power Distribution Board.

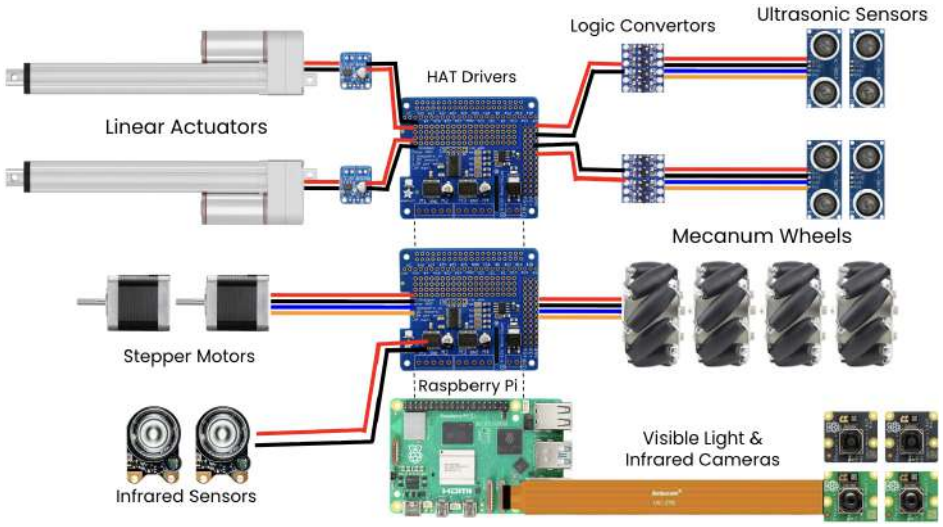


Figure 34: Simplified wiring diagram showing the connections of our Raspberry Pi, two HAT drivers, and more.

The overall side view of the vehicle is shown below **(figure 35)**.

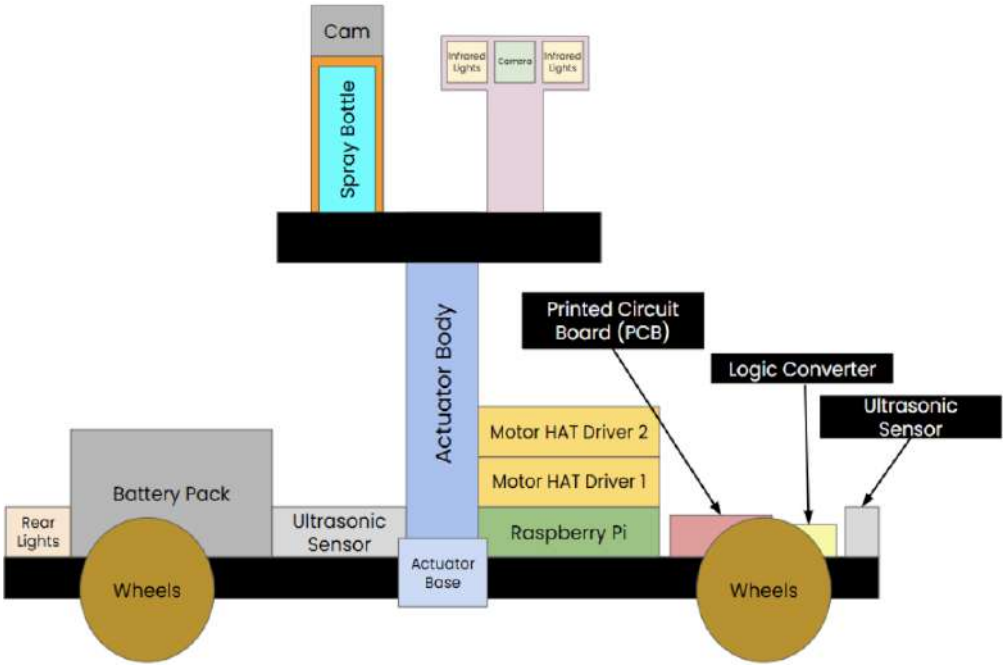


Figure 35: Side view of both platforms of the vehicle.

3.2 Vehicle Procedure

The first task that the vehicle undertakes is mapping out the field. This is crucial as building a map of the field and storing it internally in the vehicle helps it move systematically and ensures it covers the entire field. The map is represented as a 2D grid where each cell represents a small area of the field. In our case, each cell represents a 3 cm by 3 cm patch.

To determine the dimensions of the 2D grid, the user has to measure the length and width of the field and set it to those values in the program. Initially, all of the values for each cell are -1, meaning that we are not sure they are open or blocked. As the vehicle moves on and explores the field and gathers information about each cell, it updates the values of those cells to 0, representing an open space, or 1, representing a closed space.

To build this map, the vehicle uses its two forward ultrasonic sensors, which measure the distance to the nearest obstacle in the direction that the vehicle is currently facing. The vehicle is programmed to start facing north at the bottom left corner of the field. At each step, the vehicle measures the distance in front of it and uses the smaller of the two distances measured as a conservative estimate that prioritizes safety. The distance reading allows us to mark all the cells within that distance to the vehicle (in that direction) as open. If the distance indicates an obstacle is lower than the maximum distance that the sensors can detect of two meters, we will mark that spot as closed.

We then use a frontier-based exploration rule that guarantees that the vehicle will eventually scan the entire field by repeating the procedure above over and over again **(figure 36)**. At each spot that the vehicle goes to, it will rotate four times and use the ultrasonic sensor readings each time to improve efficiency. Then, to decide which spot to move to next, it defines frontiers as a free cell that is adjacent to at least one unknown cell. It chooses the nearest frontier cell to go to using a Breadth-First Search distance algorithm and physically drives there. When it gets to the new cell, the entire process repeats, where it scans the map using its ultrasonic sensors in all four directions, then determines a new cell to go to.

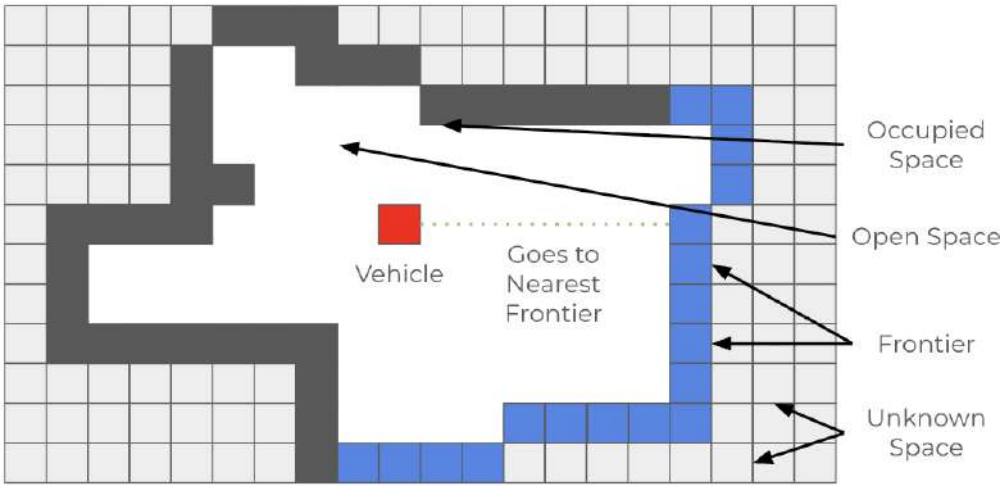


Figure 36: Workflow of the vehicle's frontier-based search process for field mapping.

Finally, after the vehicle realizes it's done mapping, either because there are no more reachable unknown cells in the 2D grid or because a safety iteration cap is reached, the vehicle returns to its starting position by reversing the exact sequence of moves it performed to get there. This procedure is important because it resets our vehicle to a consistent starting location, making it easier for repeated cycles and for the user to locate it. After this, we have a complete 2D map of the entire field.

To traverse the entire field of crops, the vehicle will use a Depth-First Search path planning approach to determine a path that visits every single open cell at least once. The vehicle will start in the same initial cell. At each cell, it will look at its neighboring cells in a fixed order. If it finds an adjacent open cell in one direction that has not been visited, it will go there. If there are no unvisited neighbors, the vehicle will return to the cell that it was on before. It will do this for every single new cell it arrives on repeatedly, until all open cells are now marked as visited. Then, it'll backtrack along its entire path once again to return to the same starting position. Throughout this entire procedure, the vehicle has stored the sequence of moves that it executed to visit each cell once, as well as the moves that it executed to return back to its starting position. Those sequences of moves performed one after another will now be the vehicle's cycle that it takes. After this step, we have determined a movement cycle that the vehicle will perform repetitively throughout its pest-management period.

While moving along the same cycle for the entire day, the vehicle will raise its linear actuators up and down fully. This makes sure that it's not just checking plants at its lowest level, but performing a comprehensive check for plants of all different heights. Throughout its entire movement process, the vehicle is always on the lookout for small objects or obstacles that aren't represented in the map that it needs to dodge. When one of its two front ultrasonic sensors detects an object that is within the set distance threshold, it will carry out a procedure to navigate around the object **(figure 37)**.

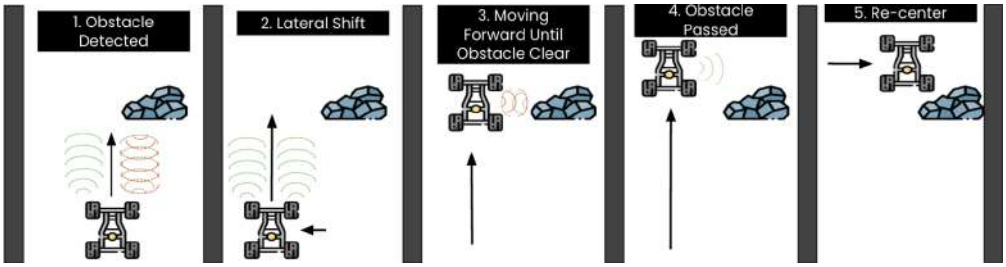


Figure 37: Vehicle movement steps when an obstacle is detected, utilizing its four ultrasonic sensors.

First, the vehicle will shift sideways incrementally until both of its front ultrasonic sensors detect that there is nothing in front of them **(Steps 1 and 2 in figure 37)**. Afterwards, it will move forward in increments until the side sensors detect an obstacle within the distance threshold **(Step 3 in figure 37)**. Then, it will move forward slightly more **(Steps 3 and 4 in figure 37)**, which means the vehicle has now moved past the object. Once the vehicle successfully clears the object, it will recenter itself by moving sideways the same distance it shifted initially. Overall, when the linear actuator and object avoidance procedures happen, the vehicle pauses its route execution to preserve route consistency.

While the vehicle is executing all of its movement, we created a separate thread in the program that runs alongside it for the vehicle's pest management procedure. While the vehicle follows along its precomputed route, it continuously monitors the field's crops for

pests using its two cameras. The frames are collected from the environment and processed in real-time, where the vehicle looks for any pest.

To detect the pests, we use a custom machine-learning pipeline designed specifically for detecting very small objects in noisy, real-world environments. Unlike standard object-detection models which perform poorly on small objects in noisy environments, our approach combines classical computer-vision techniques with deep learning to improve accuracy while remaining efficient. This entire novel machine-learning model is covered in depth in Section 4.

When pests are detected, the vehicle is then instructed to spin the motor part of the motor-cam spraying system corresponding with the camera that captured the pest. As covered in Part 1, spinning the motors on the second platform presses the cam piece into the spray bottle, spraying the MeJA solution precisely. To allow for the cameras to continuously monitor the crops for any pests even in the dark, we use two infrared LED lights for each camera. The lights automatically will turn on when the brightness drops below a certain level, allowing the vehicle to function during any time of the day. Shown at right is a recap of the key vehicle features **(figure 38)**.

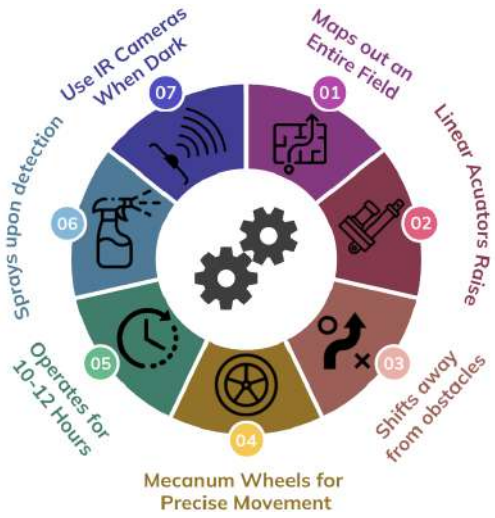


Figure 38: Summary of the vehicle's features.

4 Pest-Detection Model

Unlike conventional mass-spraying pesticide technologies, our vehicle selectively sprays the Methyl Jasmonate by only spraying the solution when pests are detected. However, current machine-learning models struggle to detect small pests in noisy, real-world environments, often producing high rates of false-positives. To address this challenge, we built a multi-phase pipeline that combines traditional feature extraction with deep learning.

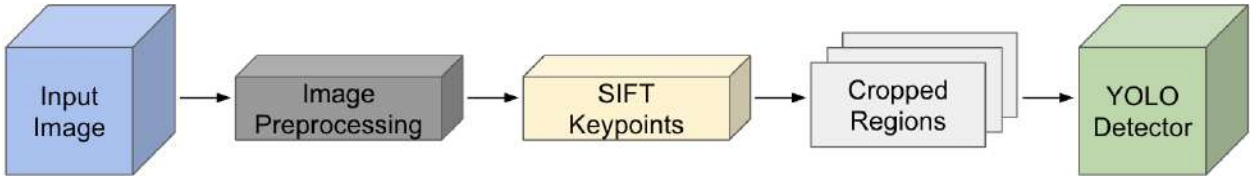


Figure 39: Simplified visual overview of the proposed model pipeline from image pre-processing and SIFT keypoint extraction to region generation and YOLOv5 detection.

The system first identifies regions of interest using SIFT-based keypoint localization, then isolates and processes these regions through a YOLO-based detector for final classification

(figure 39). This mimics human behavior, as for especially larger and more complex images, humans tend to immediately focus our attention on a few small, key areas which makes finding small objects faster and easier. After designing it, we then tested the SIFT framework on four custom metrics, and then compared the final SIFT+YOLOv5 model against other light-weight YOLOv5 add-ons, showcasing its accuracy, reliability, and efficiency.

4.1 Detection Pipeline

Given an image, the first thing our system does is convert the color to grayscale. This reduces the image from three color channels (Red-Green-Blue) down to a single black-and-white intensity image **(figure 40)**. After applying grayscale, we then use a two-stage noise filtering setup to enhance textures and edges while removing irrelevant clutter and blurriness common in noisy environments. First, a median filter with a 3x3 kernel applied to remove salt-and-pepper noise (scattered, inaccurate pixels) from the image without blurring edges. Then, a bilateral filter (with a spatial kernel of 9, sigmaColor of 75, and sigmaSpace of 75) is applied to reduce Gaussian noise, which are small fluctuations in the image commonly caused by camera sensors or environmental factors. We are now left with a clear image that will improve detection accuracy and speed.



Figure 40: Comparison of original image (left) and grayscaled image (right), demonstrating the preservation of crucial information.

We now extract keypoints from the resulting image using the Scale-Invariant Feature Transform (SIFT) algorithm, which detects interesting and crucial image regions for our model to focus on in order to find the small pests. SIFT will first build a scale space by progressively blurring the image using Gaussian kernels and subtracting these scales to create a bunch of Difference-of-Gaussians image versions. After comparing each point with 26 other neighbors to find local extrema **(figure 41)**, those candidate points then go through a process of stability refinement where low-contrast and poorly-localized points are eliminated.

Then, SIFT will represent each keypoint with a 128-dimensional descriptor capturing the patterns and characteristics of each point, which we can use later to identify our target objects like pests. Because this process is computationally intensive, we cap the number of identified keypoints at 150 to 200 per image to significantly reduce processing time, prioritizing the

points with the highest evaluated scores.

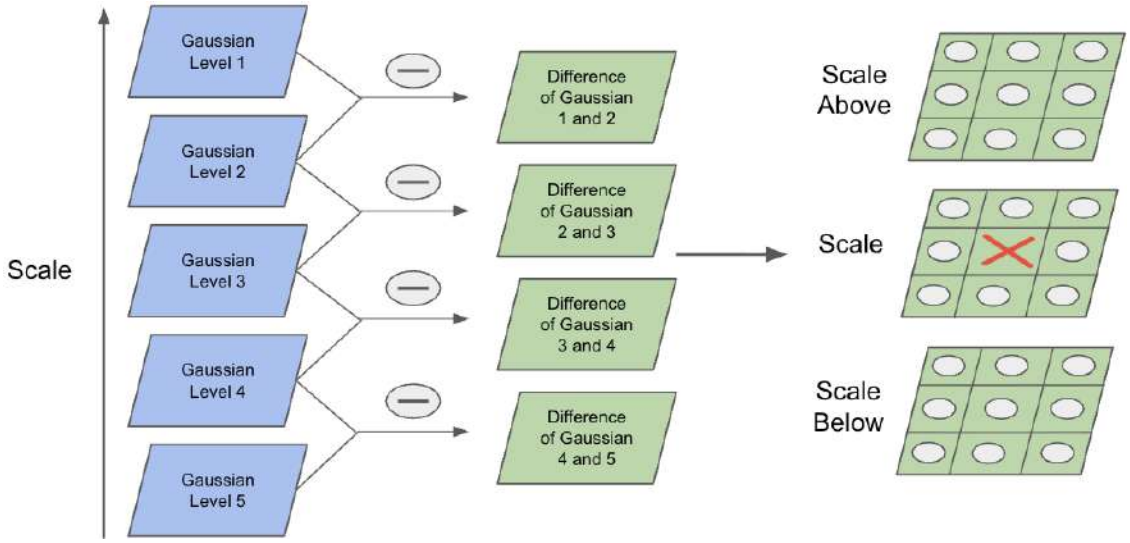


Figure 41: Illustration of SIFT's difference-of-gaussians process (left) and finding local extrema across scales (right) for keypoint detection.

Once the keypoints are extracted, we apply a two-step filtering process to refine their relevance and heavily reduce SIFT's false positives. First, we calculate the Shannon entropy of an 11x11 patch around each keypoint. The entropy here quantifies the amount of local texture variation, with regions that have higher entropy being more likely to represent something meaningful. Keypoints that fall below the 65th percentile of entropy scores are then discarded, eliminating those in visually uniform areas.

However, to avoid overly aggressive filtering that could eliminate accurate keypoints, we applied an edge-based restoration step using a Canny edge map to restore some of the already eliminated keypoints. The edge detector identifies edges by locating regions of rapid intensity change, which it does by using gradient magnitude and non-maximum suppression to produce thin, well-localized contours.

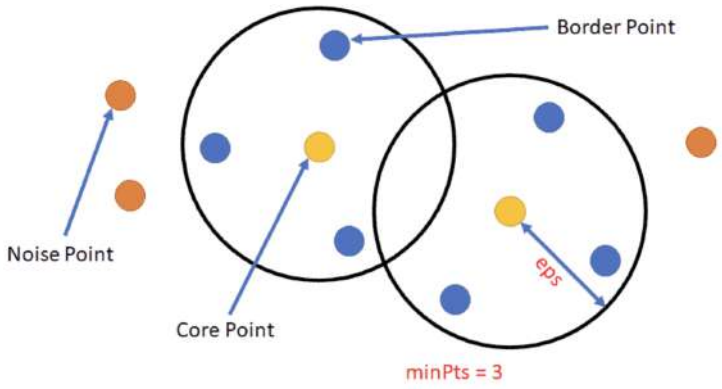


Figure 42: Illustration of DBSCAN clustering with border, core, and noise points.
Source: Reproduced from Gour, 2023

Any filtered keypoints that coincide with strong edges are reinstated, as edges often delineate object boundaries even if their overall entropy is low. With this additional filtering process, we are now left with a set of promising points in areas of high interest.

Now, the remaining keypoints are grouped into candidate regions using the Density-Based Spatial Clustering of Applications with Noise (DBSCAN) **(figure 42)**. DBSCAN clusters keypoints based on spatial density, with us requiring a minimum of three points within an epsilon radius of 75 pixels of a core point to form a cluster. After constructing multiple clusters, the remaining few points are then treated as noise. For each cluster, we compute the bounding box by taking the minimum and maximum x- and y-coordinates of its keypoints. The score of each cluster is then defined as the sum of its associated entropy values.

Clusters are then ordered from the highest score to the lowest score, and a non-maximum suppression (NMS)-like step is applied to ensure that only non-overlapping, high-value boxes remain. The number of boxes will then usually range anywhere from one to three, with these boxes finally being passed to YOLOv5 for the final object detection. Now, the YOLOv5 model only needs to focus on the regions that it has been given, which is supposed to increase its accuracy at detecting smaller objects.

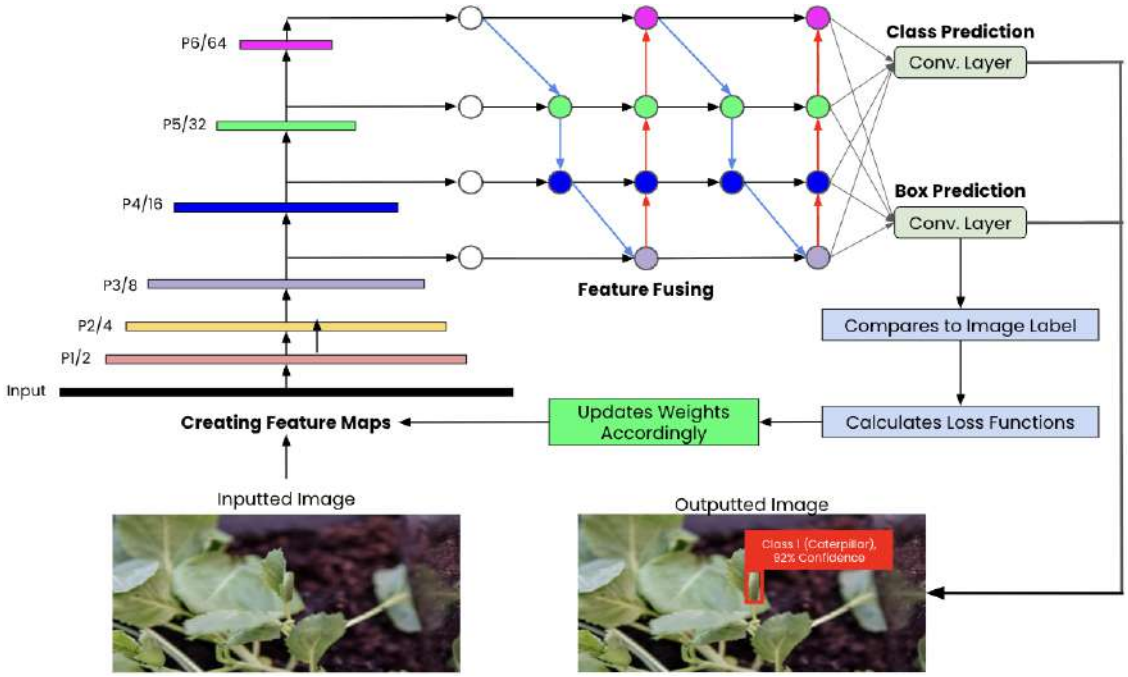


Figure 43: Overview the YOLOv5 model on sample input/output with feature extraction, feature fusion, and prediction heads on sample input/output.

The final detection leverages the You Only Look Once (YOLOv5s) model **(figure 43)** to classify and localize objects within the candidate regions produced prior. Each bounding box will be applied with an adaptive padding of 0.05 proportional to the box size to ensure the target object is fully covered, and will then be cropped out of the original images.

These cropped regions are then passed in one-by-one through the YOLOv5, which uses a convolutional backbone and feature pyramid network (FPN) to extract multiscale features. Over time through training, it associates features with certain objects and differentiate target objects (like pests) from other objects. We further use the small model (YOLOv5s) to balance speed and accuracy.

The model is pre-trained on the Common Objects in Context (COCO) dataset and then fine-tuned on our own custom image datasets. During training, data augmentation (including random scaling, flipping, and mosaic augmentation) was implemented to improve its robustness and prevent overfitting. The trained model will finally output the object classifications and refined bounding boxes for each cropped region. This entire process ultimately yields a pest-detection system that balances computational efficiency with robust small-object detection.

4.2 Model Testing

To prepare, we gathered many images of all different kinds of common everyday objects. These were taken either from Google Images or from Adobe Stock image collections. Some photos were also taken by us. All numbers indicating tested results were obtained by averaging numerous trials with a fixed amount for each number in that chart. Overall, we decided to not only test our model on pests, but also on a variety of everyday objects to prove its generalization capability.

First, we test our SIFT-based framework (which excludes the actual detection step) on how well it was able to localize small objects. To do this, we came up with four custom metrics to assess the framework on:

- Single Box Accuracy (SBA): This measures the percentage of all generated boxes that actually cover the target objects.
- Target Coverage Ratio (TCR): This measures the percentage of all labeled objects where at least one box covered the target, enabling the possibility of a detection.
- Bounding Box Mismatch (BBM): This measures the area of the bounding box of the object that is covered over the area of all the generated boxes combined.
- Object to Box Area Ratio (OBR): This measures the area of the bounding box of an object that is covered by the single best box over the area of that box.

We decided to test it on three types of objects. First, we picked cars because of their contrast and textured appearance. On the contrary, we picked caterpillars due to their minimal contrast and smooth bodies. Finally, we picked common miscellaneous items that had both properties to ensure a diverse dataset. For each type, we then manipulated a portion of them by changing the lighting and adding blur to challenge our method's robustness. For each of the 9 types of tests below, we used 25 images of that kind **(figure 44)**.

Image Dataset	SBA (%)	TCR (%)	BBM (%)	OBR (%)
Vehicle - Normal	**93.5**	**100.0**	65.3	71.7
Vehicle - Lighting	89.1	**100.0**	63.3	66.9
Vehicle - Blurriness	91.3	**100.0**	63.9	71.6
Caterpillar - Normal	60.0	98.0	43.4	66.8
Caterpillar - Lighting	**56.0**	**94.0**	40.9	65.1
Caterpillar - Blurriness	**56.0**	98.0	**40.6**	**62.6**
Miscellaneous - Normal	88.0	98.7	**77.0**	**82.0**
Miscellaneous - Lighting	90.0	92.7	76.4	81.0
Miscellaneous - Blurriness	90.0	96.7	75.6	81.4

Figure 44: Assessment of SIFT-based framework's accuracy using four custom-made metrics among different images and manipulations. Blue/red respectively mark the best/worst results for each metric.

Our method was able to achieve exceptionally high accuracy on TCR for everything, which means that in almost all cases, there was at least one box covering the object. Almost all of the time, the SIFT framework would generate around 1-3 boxes capturing areas of high interest, with one actually hitting the target, leading to 50-60% SBA for caterpillars. Shown are examples of our SIFT framework producing high-interest boxes on caterpillar images **(figure 45)**.



Figure 45: Example detections from the framework on zoomed-in caterpillar images, showing bounding boxes accurately localizing targets in all scenarios.

For vehicles and miscellaneous images which usually had more contrast and complexity, our model would almost always draw a single box around the object of interest, leading to very high SBA scores. This ensures full coverage on images with multiple complex parts

while accepting slight redundancy to increase TCR accuracy. For the most part, the box that covered the object managed to cover it completely with minimal padding around it as shown in the OBR and BBM scores, giving an accurate cropped image.

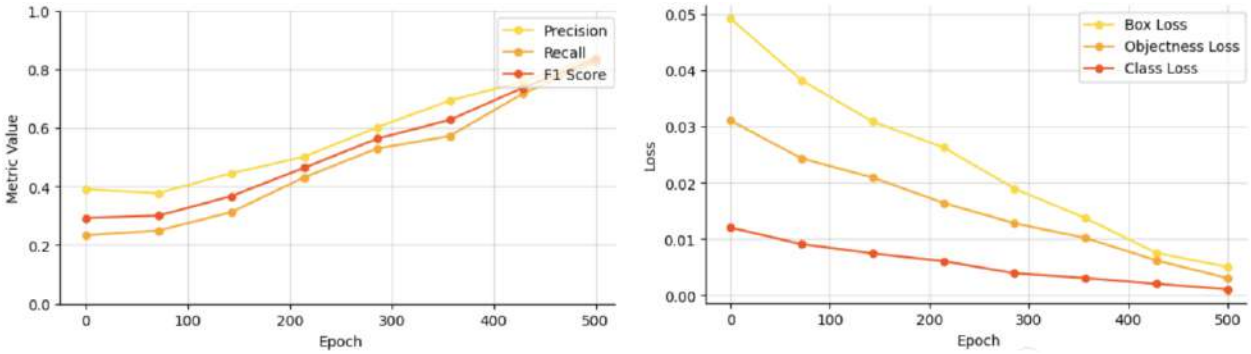


Figure 46: Graphs of default metrics (left) and loss functions (right) of custom-trained YOLOv5 model during training over 500 epochs.

Now, we aim to test the effectiveness of our combined model against other popular choices for small object detection. We decided to train a YOLOv5 on hundreds of images over hundreds of epochs to detect caterpillars specifically, with each add-on being appended to that exact same base model. Each image was labeled in a Jupyter Notebook and then checked for labeling inaccuracies again. We also included image augmentation for our training datasets and documented the progress over 500 epochs **(figure 46)**. This included tracking precision, recall, F1 score, as well as the box loss, object loss, and class losses for accuracy. Note that these metrics were generated during the training process and may be different from their traditional definitions.

Now, we employ YOLOv5 on the regions that our previous SIFT-based framework found for each image. We then compare these with other prominent models that can easily be added onto YOLOv5. These combined models are:

- YOLOv5 itself: This is the baseline and goes through a single pass on each image before reaching a bounding box conclusion.
- YOLOv5 with Multi-Scale Inference (MSI): Rather than evaluating every image on a fixed size, MSI runs an inference on multiple resized versions of the same image. YOLOv5 will then make predictions for each version, which allow it to capture objects that are easier to spot at different resolutions. The predictions are then merged to produce a final result.
- YOLOv5 with Test-Time Augmentation (TTA): Instead of giving YOLOv5 only one pass for each image, TTA applies augmentation on each image to generate multiple similar copies of that image by rotating, flipping, etc. It then allows YOLOv5 to make predictions on each generated sample and merges the predictions at the end for a more reliable result.

- YOLOv5 with Slicing Aided Hyper Inference (SAHI): SAHI first divides a larger image into many smaller images with slight overlap to avoid splitting larger objects (like a sliding window). Then, like TTA and MSI, it sends these smaller images to YOLOv5 for it to evaluate every single one. This makes smaller objects appear more prominent in each sliced image, improving accuracy.

We now test the performances of each of these models on small, medium, and large objects **(figure 47)**. In a 640 pixel by 640 pixel image, small objects (S) here are defined as having their maximum side length smaller than or equal to 32 pixels ($\frac{1}{20}$ of a side of the image), medium objects (M) have their maximum side length range from 32 to 128 pixels ($\frac{1}{20}$ to $\frac{1}{5}$ of a side of the image), and large objects (L) have their maximum side length larger than 128 pixels (over $\frac{1}{5}$ of a side of the image).

For each object size, we then evaluated the different models on five common metrics, namely Precision, Recall, F1 Score, Confidence, and IoU. We did our own calculations (rather than using existing packages) to ensure consistency in the definitions of Precision, Recall, and F1. We also made two new metrics. Confidence is the average confidence score of all true positive detections. IoU is the average intersection over union score of true positives, or how well the predicted box matches the object box.

Model	Precision	Recall	F1	Confidence	IoU
YOLOv5s - S	13.3	**16.0**	14.0	48.1	25.6
YOLOv5s + MSI - S	15.0	28.0	18.1	51.4	49.9
YOLOv5s + TTA - S	**8.7**	24.0	**12.5**	**47.1**	**25.2**
YOLOv5s + SAHI - S	25.6	72.0	32.9	**85.7**	**79.3**
Created Model - S	**70.0**	**90.0**	**76.0**	73.9	75.8
YOLOv5s - M	61.7	76.0	65.6	71.9	**69.2**
YOLOv5s + MSI - M	66.7	**68.0**	67.2	**84.8**	86.2
YOLOv5s + TTA - M	**47.5**	76.0	**55.0**	**70.9**	75.5
YOLOv5s + SAHI - M	69.3	90.0	72.6	83.7	78.4
Created Model - M	**96.0**	**98.0**	**97.0**	81.3	**83.5**
YOLOv5s - L	74.7	94.0	80.4	80.8	**79.0**
YOLOv5s + MSI - L	85.3	90.0	86.9	**86.9**	**85.7**
YOLOv5s + TTA - L	**71.3**	**86.0**	**75.7**	86.7	84.6
YOLOv5s + SAHI - L	87.6	**96.0**	89.6	83.3	81.6
Created Model - L	**92.0**	**96.0**	**93.3**	**77.2**	84.3

Figure 47: Accuracy of different types of small object detection tools with YOLOv5 on five standardized metrics, showing the custom model achieving the best performances across each object size. Blue/red numbers are the best/worst performances in each box.

Below is our model on some example caterpillar images used in the testing **(figure 48)**.

The data and figures illustrate our combined model's ability to accurately identify extremely small pests even in visually dense environments filled with numerous leaves, shadows, and background clutter. This ability shows our model's potential to enable our vehicle to detect pests and accurately locate them in noisy, real-world environments.

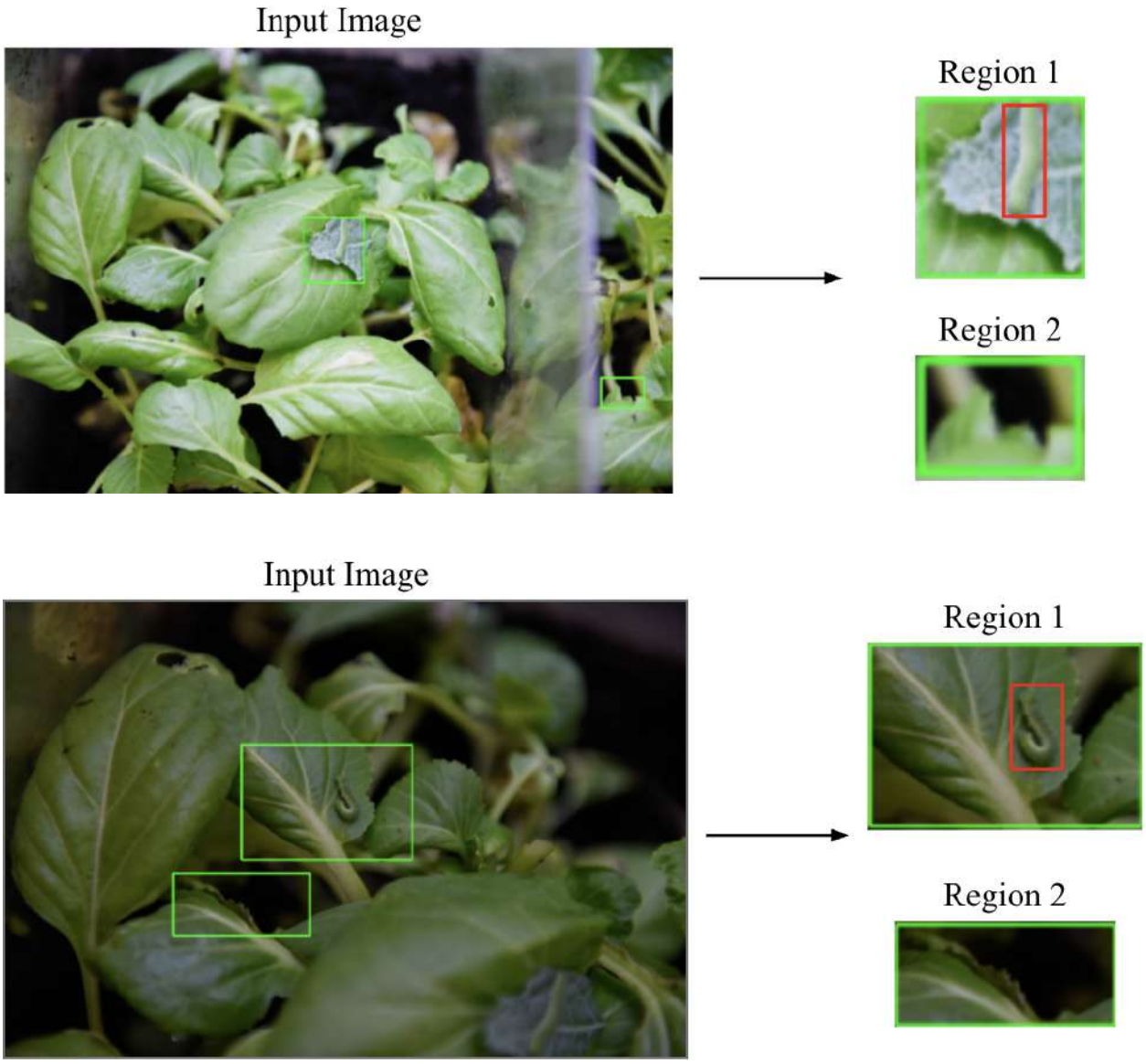


Figure 48: Two-step example workflow of custom SIFT-YOLOv5 model on small caterpillar images.

Now, we test the efficiency of the five models **(figure 49)**, which we did this by setting time markers in the code for five major portions of our method. The numbers below are the averages after feeding in numerous images. Once again, we tested them on Google Colab where it ran on their CPUs, and a Raspberry Pi 5 by running it locally. The images we used to test were around 1000-2000 pixels on each side.

System Portion	Average (ms)	Median (ms)	Std. Dev. (ms)
YOLOv5s - CPU	329.0	305.1	92.6
YOLOv5s + MSI - CPU	2380.9	2274.8	508.7
YOLOv5s + TTA - CPU	3104.2	3483.8	878.7
YOLOv5s + SAHI - CPU	**6020.3**	**6164.1**	3763.9
Created Model - CPU	**740.5**	**735.1**	380.5
YOLOv5s - RPi	412.5	411.7	51.0
YOLOv5s + MSI - RPi	2854.1	2590.5	523.0
YOLOv5s + TTA - RPi	3353.6	3419.8	631.7
YOLOv5s + SAHI - RPi	**6484.0**	**6859.4**	3965.3
Created Model - RPi	**821.7**	**816.1**	402.9

Figure 49: Speeds of different small object detection tools on CPUs and a Raspberry Pi 5, highlighting our model's efficiency and the un-viable speeds of others.

Overall, these results show that our model is both highly accurate across a wide range of object sizes (especially small objects like pests) and consistently faster than competing add-on methods, achieving strong performances in both accuracy and efficiency. Integrating this model into our vehicle allows for the accurate detection of pests, and therefore, the precise application of MeJA.

5 Conclusion

This project developed a novel sustainable pest-control approach by pairing a biological alternative to traditional pesticides with an autonomous deployment mechanism. In the biology phase, we first found that exogenous Methyl Jasmonate can significantly reduce pest damage and insect survival, but that it overall severely stunted plant growth. To reduce this tradeoff, we used dsRNA to target the growth-suppressing *GA2ox3/7* genes, and packaged it in carbon dot nanocarriers to improve its stability. Then, to apply this MeJA and dsRNA formulation, we designed an autonomous vehicle that can navigate for long durations and selectively apply the solution only when pests were detected. To accurately detect pests, we designed a multi-phase detection pipeline that mimics human behavior to primarily focus on interesting regions in an image.

The main limitation of this work is that the deployment vehicle we've completed is currently only functional in controlled, indoor environments. Real agricultural environments introduce many new challenges like uneven terrain, adverse weather, and larger environments that our vehicle isn't able to adapt to. Therefore, our next steps focus on building a new large-scale vehicle version with a more robust navigation system, stronger materials, higher-quality sensing and computation, along with testing it through numerous trials in real-world settings.

6 References

*All images, photographs, and diagrams, unless otherwise cited, were created/taken entirely by the applicant

1. Acharya, A. (2024, November 5). Slicing aided hyper inference (SAHI) for small object detection: Explained. Encord. https://encord.com/blog/slicing-aided-hyper-inference-explained/

2. Adafruit Industries, Ada, Lady. (2025). Adafruit DC and Stepper Motor HAT for Raspberry Pi. https://cdn-learn.adafruit.com/downloads/pdf/adafruit-dc-and-stepper-motor-hat-for-raspberry-pi.pdf

3. Akbarnezhad, E., Naserizadeh, F. (2024). Improving camouflage object detection using U-Net and VGG16 deep neural networks and CBAM attention mechanism. 2024 10th International Conference on Artificial Intelligence and Robotics (QICAR), 56–62. https://doi.org/10.1109/qicar61538.2024.10496615

4. Akyon, F. C., Altinuc, S. O., Temizel, A. (2022). Slicing aided hyper inference and fine-tuning for small object detection. 2022 IEEE International Conference on Image Processing (ICIP), 989–993. https://doi.org/10.1109/ICIP46576.2022.9897990

5. Applicability of Mecanum wheeled platforms/robots in military field. (n.d.). ResearchGate. https://www.researchgate.net/figure/Applicability-of-Mecanum-wheeled-platforms-robots-in-military-field_tbl1_361818403

6. Betalight Tactical. (2025, November 18). What is Infrared LED Lighting? Betalight-tactical. https://betalight-tactical.com/knowledge-base/led/what-is-infrared-led-lighting

7. Building a robot that can avoid obstacles (Post 15). (2025, October 1). Arduino Forum. https://forum.arduino.cc/t/building-a-robot-that-can-avoid-obstacles/1369928/15

8. Codecademy Team. (n.d.). Breadth-First Search (BFS) algorithm explained. Codecademy. https://www.codecademy.com/article/breadth-first-search-bfs-algorithm

9. Delgado-Martín, J., Delgado-Olidén, A., Velasco, L. (2022). Carbon dots boost DSRNA delivery in plants and increase local and systemic SIRNA production. International Journal of Molecular Sciences, 23(10), 5338. https://doi.org/10.3390/ijms23105338

10. Dubrovina, A. S., Kiselev, K. V. (2019). Exogenous RNAs for gene regulation and plant resistance. International Journal of Molecular Sciences, 20(9), 2282. https://doi.org/10.3390/ijms20092282

11. Durai, P. (2023, December 29). Exploring SAHI: Slicing aided hyper inference for small object detection. LearnOpenCV. https://learnopencv.com/slicing-aided-hyper-inference/

12. Edge AI and Vision Alliance. (2024, June 19). Understanding spatial noise and its reduction methods using convolution. https://www.edge-ai-vision.com/2024/06/understanding-spatial-noise-and-its-reduction-methods-using-convolution/

13. Erb, M., Kliebenstein, D. J. (2020). Plant secondary metabolites as defenses, regulators, and primary metabolites: the blurred functional trichotomy. PLANT PHYSIOLOGY, 184(1), 39–52. https://doi.org/10.1104/pp.20.00433

14. Fukazawa, J., Mori, K., Ando, H., Mori, R., Kanno, Y., Seo, M., Takahashi, Y. (2023). Jasmonate inhibits plant growth and reduces gibberellin levels via microRNA5998 and transcription factor MYC2. PLANT PHYSIOLOGY, 193(3), 2197–2214. https://doi.org/10.1093/plphys/kiad453

15. GeeksforGeeks. (2025a, July 4). DBSCAN clustering in ML – Density based clustering. https://www.geeksforgeeks.org/machine-learning/dbscan-clustering-in-ml-density-based-clustering/

16. GeeksforGeeks. (2025b, July 11). Python: Grayscaling of images using OpenCV. https://www.geeksforgeeks.org/python/python-grayscaling-of-images-using-opencv/

17. GeeksforGeeks. (2025, October 3). Multithreading in Python. GeeksforGeeks. https://www.geeksforgeeks.org/python/multithreading-python-set-1/

18. GeeksforGeeks. (2025, October 25). Depth first search or DFS for a graph. https://www.geeksforgeeks.org/dsa/depth-first-search-or-dfs-for-a-graph/

19. Heil, M., Ton, J. (2008). Long-distance signalling in plant defence. Trends in Plant Science, 13(6), 264–272. https://doi.org/10.1016/j.tplants.2008.03.005

20. How to use Stepper Motors and DC Motors with a Raspberry Pi - Adafruit DC Stepper Motor HAT. (n.d.). Core Electronics. https://core-electronics.com.au/guides/raspberry-pi-dc-stepper-motor-guide/

21. Hut, P. (2023, May 4). HC-SR04 Ultrasonic Range sensor on the Raspberry Pi. The Pi Hut. https://thepihut.com/blogs/raspberry-pi-tutorials/hc-sr04-ultrasonic-range-sensor-on-the-raspberry-pi

22. Ito, T., Okada, K., Fukazawa, J., Takahashi, Y. (2018). DELLA-dependent and -independent gibberellin signaling. Plant Signaling Behavior, 13(3), e1445933. https://doi.org/10.1080/15592324.2018.1445933

23. Jensen, D. (2024, May 6). Cam systems and cam design. Introduction to Mechanical Design and Manufacturing. https://uark.pressbooks.pub/mechanicaldesign/chapter/cam-systems-and-cam-design/

24. Jin, G., Qi, J., Zu, H., Liu, S., Gershenzon, J., Lou, Y., Baldwin, I. T., Li, R. (2023). Jasmonate-mediated gibberellin catabolism constrains growth during herbivore attack in rice. The Plant Cell, 35(10), 3828–3844. https://doi.org/10.1093/plcell/koad191

25. Jin, Z., Qu, P., Sun, C., Luo, M., Gui, Y., Zhang, J., Liu, H. (2021). DWCA-YOLOv5: An improved single shot detector for safety helmet detection. Journal of Sensors, 2021(1). https://doi.org/10.1155/2021/4746516

26. Keita, Z. (2023, November 14). An introduction to convolutional neural networks: A comprehensive guide to CNNs in deep learning. Datacamp. https://www.datacamp.com/tutorial/introduction-to-convolutional-neural-networks-cnns

27. Kennerley, M. (2021, May 21). A comparison of SIFT, SURF and ORB on OpenCV.

Medium. https://mikhail-kennerley.medium.com/a-comparison-of-sift-surf-and-orb-on-opencv-59119b9ec3d0

28. Khanam, R., Hussain, M. (2024). What is YOLOv5: A deep look into the internal features of the popular object detector. arXiv. https://doi.org/10.48550/arXiv.2407.20892

29. Kimura, M. (2024). Understanding test-time augmentation. arXiv. https://doi.org/10.48550/arXiv.2402.06892

30. Koch, A., Biedenkopf, D., Furch, A., Weber, L., Rossbach, O., Abdellatef, E., Linicus, L., Johannsmeier, J., Jelonek, L., Goesmann, A., Cardoza, V., McMillan, J., Mentzel, T., Kogel, K. (2016). An RNAi-Based Control of Fusarium graminearum Infections Through Spraying of Long dsRNAs Involves a Plant Passage and Is Controlled by the Fungal Silencing Machinery. PLoS Pathogens, 12(10), e1005901. https://doi.org/10.1371/journal.ppat.1005901

31. Lin, T.-Y., Maire, M., Belongie, S., Hays, J., Perona, P., Ramanan, D., Dollár, P., Zitnick, C. L. (2014). Microsoft COCO: Common objects in context. Lecture Notes in Computer Science, 740–755. https://doi.org/10.1007/978-3-319-10602-1_48

32. Lu, S., Guo, S., Xu, P., Li, X., Zhao, Y., Gu, W., Xue, M. (2016). Hydrothermal synthesis of nitrogen-doped carbon dots with real-time live-cell imaging and blood-brain barrier penetration capabilities. International Journal of Nanomedicine, Volume 11, 6325–6336. https://doi.org/10.2147/ijn.s119252

33, M., T. (2024, September 20). What is scale-invariant feature transform (SIFT)? Roboflow Blog. https://blog.roboflow.com/sift/

34. M., T. (2025, May 30). Edge detection in image processing: An introduction. Roboflow Blog. https://blog.roboflow.com/edge-detection/#canny-edge-detection

35. Mesa, P. G. (2024, June 10). Understanding YOLOv5 loss: A comprehensive analysis. Medium. https://pgmesa.medium.com/understanding-yolov5-loss-a-comprehensive-analysis-ffe35e6203e0

36. Mousavi, V., Varshosaz, M., Remondino, F. (2021). Using information content to select keypoints for UAV image matching. Remote Sensing, 13(7), 1302. https://doi.org/10.3390/rs13071302

37. NEB. (n.d.). INSTRUCTION MANUAL HISCrIBe T7 High yield RNA Synthesis Kit. https://www.neb.com/en-us/-/media/nebus/files/manuals/manuale2040.pdf

38. Pagano, M., Lunetta, E., Belli, F., Mocarli, G., Cocozza, C., Cacciotti, I. (2025). Advancements in Agricultural Nanotechnology: An updated review. Plants, 14(18), 2939. https://doi.org/10.3390/plants14182939

39. Pauwels, L., Goossens, A. (2011). The JAZ proteins: a crucial interface in the jasmonate signaling cascade. The Plant Cell, 23(9), 3089–3100. https://doi.org/10.1105/tpc.111.089300

40. Praharsha, C. H., Poulose, A. (2024). CBAM VGG16: An efficient driver distraction classification using CBAM embedded VGG16 architecture. Computers in Biology and Medicine, 180, 108945. https://doi.org/10.1016/j.compbiomed.2024.108945

41. Praveen, S., Jung, Y. (2025). CBAM-STN-TPS-YOLO: Enhancing agricultural object detection through spatially adaptive attention mechanisms. arXiv. https://doi.org/10.48550/arXiv.2506.07357

42. Prem. (2025, August 19). Revolutionizing Pest Control with Pesticide Spraying Drone Technology. Marut Drones. https://marutdrones.com/revolutionizing-pest-control-with-pesticide-spraying-drone-technology/

43. Raspberry Pi Camera Module 3 - WaveShare Wiki. (n.d.). https://www.waveshare.com/wiki/Raspberry_Pi_Camera_Module_3

44. Schwartz, S. H., Hendrix, B., Hoffer, P., Sanders, R. A., Zheng, W. (2020). Carbon dots for efficient small interfering RNA delivery and gene silencing in plants. PLANT PHYSIOLOGY, 184(2), 647–657. https://doi.org/10.1104/pp.20.00733

45. Solawetz, J., Kondrackis, L. (2024, September 5). How to detect small objects: A guide. Roboflow Blog. https://blog.roboflow.com/detect-small-objects/#why-is-the-small-object-problem-hard-to-solve

46. Song, C., Cao, Y., Dai, J., Li, G., Manzoor, M. A., Chen, C., Deng, H. (2022). The Multifaceted Roles of MYC2 in plants: toward transcriptional reprogramming and stress tolerance by Jasmonate signaling. Frontiers in Plant Science, 13, 868874. https://doi.org/10.3389/fpls.2022.868874

47. SparkFun Learn. (n.d.). Bi-Directional Logic Level Converter Hookup Guide. https://learn.sparkfun.com/tutorials/bi-directional-logic-level-converter-hookup-guide/all

48. Swain, A. (2020, July 16). Noise filtering in digital image processing. Medium. https://medium.com/@anishaswain/noise-filtering-in-digital-image-processing-d12b5266847c

49. Swift, N. W. (2017, February 27). Easy A (star) pathfinding*. Medium. https://medium.com/@nicholas.w.swift/easy-a-star-pathfinding-7e6689c7f7b2

50. Tian, Y., Ye, Q., Doermann, D. (2025). YOLOv12: Attention-centric real-time object detectors. arXiv. https://doi.org/10.48550/arXiv.2502.12524

51. Topiwala, A., Inani, P., Kathpal, A. (2018, June 10). Frontier based exploration for autonomous robot. arXiv.org. https://arxiv.org/abs/1806.03581

52. Uni Matrix Zero. (2024, October 1). How to measure entropy in images with Python. https://unimatrixz.com/blog/latent-space-image-quality-with-entropy/

53. Voltaat Learn. (n.d.). How to control a stepper motor with raspberry pi 5? https://learn.voltaat.com/tutorials/how-to-control-a-stepper-motor-with-raspberry-pi-5

54. Voltaat Learn. (n.d.). How to use Ultrasonic Sensor with Raspberry pi 5? https://learn.voltaat.com/tutorials/how-to-use-ultrasonic-sensor-with-raspberry-pi-5

55. Wang, M., Weiberg, A., Lin, F., Thomma, B. P. H. J., Huang, H., Jin, H. (2016). Bidirectional cross-kingdom RNAi and fungal uptake of external RNAs confer plant protection. Nature Plants, 2(10), 16151. https://doi.org/10.1038/nplants.2016.151

56. WelkinU. (n.d.). Among Us player tracking with YOLOv5 and SIFT [Computer software]. GitHub. https://github.com/WelkinU/AmongUsPlayerTracker

57. What is a linear actuator? - Learn how they work here. (n.d.). Linak. https://www.linak-us.com/products/linear-actuators/what-is-a-linear-actuator/

58. Woo, S., Park, J., Lee, J.-Y., Kweon, I. S. (2018). CBAM: Convolutional block attention module. Lecture Notes in Computer Science, 3–19. https://doi.org/10.1007/978-3-030-01234-2_1

59. Zander, M., Lewsey, M. G., Clark, N. M., Yin, L., Bartlett, A., Guzmán, J. P. S., Hann, E., Langford, A. E., Jow, B., Wise, A., Nery, J. R., Chen, H., Bar-Joseph, Z., Walley, J. W., Solano, R., Ecker, J. R. (2020). Publisher Correction: Integrated multi-omics framework of the plant response to jasmonic acid. Nature Plants, 6(8), 1065. https://doi.org/10.1038/s41477-020-0743-y